

# High-Entropy Alloys as a Platform for Catalysis: Progress, Challenges, and Opportunities

Yue Xin,<sup>II</sup> Shuhui Li,<sup>II</sup> Yayang Qian,<sup>II</sup> Wenkun Zhu, Haibo Yuan, Pengyan Jiang, Ruihan Guo, and Liangbing Wang<sup>\*</sup>



Cite This: *ACS Catal.* 2020, 10, 11280–11306



Read Online

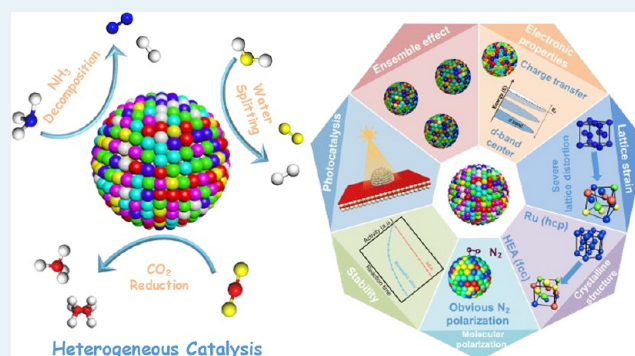
ACCESS |

Metrics & More

Article Recommendations

**ABSTRACT:** High-entropy alloys (HEAs), which are defined as near-equimolar alloys of five or more elements, are attracting ever increasing attention because of the unique properties in a variety of applications. Recently, HEAs have already exhibited remarkable catalytic performance toward several thermal-driven and electrocatalytic reactions. HEAs not only regulate the electronic and geometric structures to a large degree but also serve as a platform to construct catalysts with unexpected performance. Herein, recent advances regarding HEA-based catalysis are systematically summarized, with a special focus on the synthetic methods for HEA-based catalysts, catalytic performance, and mechanistic understanding. Moreover, the challenges and future opportunities for this research area are carefully discussed. A series of open questions and promising directions to be explored are proposed, including synthetic methods, regulation of electronic properties, identification of active centers, and applications into photocatalysis. This Review provides an overview about the progress, challenges, and opportunities for HEA-based catalysis.

**KEYWORDS:** *high-entropy alloys, heterogeneous catalysis, electrocatalysis, photocatalysis, synthetic methods, electronic properties, d-band center, active centers*



## 1. INTRODUCTION

Since the first report on crystalline high-entropy alloys (HEAs) published in 2004, the research on HEAs has attracted tremendous interest over the past 16 years.<sup>1,2</sup> Actually, the research background can also be traced back to the research on amorphous alloys (also known as metallic glass) with high mixed entropy in the 1990s.<sup>3–6</sup> In the early days, HEAs are limitedly defined as alloys composed of five or more elemental components in equimolar ratios. Nevertheless, it is found that there is not necessary to restrict the concentration of elemental components in HEAs with the deep insight into related research.<sup>1,2,7,8</sup> The properties of HEAs are significantly regulated by tuning the metallic component. At present, the definition of HEAs is still controversial. There are mainly two definitions of HEAs based on composition and entropy (i.e., the composition-based definition and entropy-based definition). For the composition-based definition, HEAs refer to the alloys composed of five or more elemental components, with the concentration of each element being between 5 and 35 atomic percentage (at.%).<sup>7,9</sup> The entropy-based definition identifies HEAs via the mixed configuration entropy ( $S$ ). The mixed configuration entropy of HEAs is able to be depicted by the following equation:

$$S = -R \sum x_i \ln(x_i) \quad (1)$$

where  $R$  is the molar gas constant, and  $x_i$  represents the mole fraction of the elemental component.<sup>2,8</sup> As such,  $S$  of HEAs with equal molar ratios for metallic elements in liquid state or solid-solution state can be simplified:

$$S = R \ln(n) \quad (2)$$

where  $n$  represents the number of components in the alloy.<sup>2,8</sup> For the alloy with the number of elemental components  $\geq 5$ , the alloy with mixed configuration entropy  $S \geq 1.5R$  refers to a HEA.<sup>7,9,10</sup> Particularly, the alloy with  $S \geq 1.36R$  is also identified as a HEA for quaternary alloy.<sup>7,9,11,12</sup> These two definitions of HEAs encompass a wide range of alloys based on the composition and entropy, and overlap in most cases. In this Review, we focus on HEAs that fit any of the definitions above.

**Received:** August 18, 2020

**Revised:** September 2, 2020

**Published:** September 17, 2020



Thanks to the efforts from a variety of groups, the properties and characteristics of HEAs are deeply investigated and systematically summarized, as shown in Figure 1. (i) *The high entropy effect*

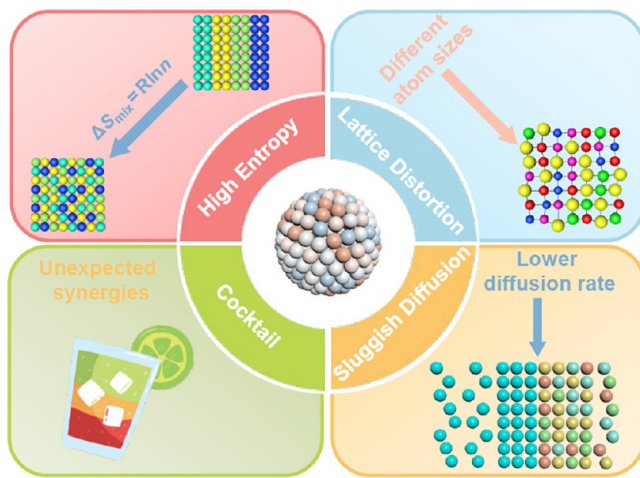


Figure 1. Schematic illustration of the properties and characteristics of HEAs.

*entropy effect* is usually a qualitative comparison concept, referring to the enhanced mixed configuration entropy of HEAs relative to that of pure metals and intermetallic compounds.<sup>2</sup> As the number of components increase, the mixed configuration entropy will also increase based on eqs 1 and 2. The elevation of mixed configuration entropy benefits to the formation of a stable single-phase solid solution structure rather than a fragile intermetallic compound, as well as directly contributes to the excellent stability of HEAs.<sup>13,14</sup> (ii) *The lattice distortion effect* is generated because of the large difference in the sizes of atoms forming each component that comprise HEAs. The random occupation of metallic atoms in a crystalline lattice results in severe lattice distortion.<sup>15</sup> This severe lattice distortion not only significantly promotes the hardness of HEAs but also reduces the electrical and thermal conductivity.<sup>16</sup> (iii) *The sluggish diffusion effect* is highly related to a lattice distortion effect. A serious lattice distortion in HEAs is considered to raise the energy barrier of atomic diffusion.<sup>17</sup> This effect also contributes to the formation of nanoscale HEAs due to the hindrance of atomic diffusion on the surface.<sup>18–21</sup> (iv) *The cocktail effect* means that the synergistic response among the various element components in HEA will give rise to various unexpected properties.<sup>7,15</sup> The overall density of HEAs decreases when the components are mostly light elements, while amazing antioxidant activity is achieved after introducing a metallic element with strong oxidative resistance.<sup>15</sup> Such synergies are also widely reflected in thermo-electric response, mechanical properties, and magnetic behaviors.<sup>22–26</sup>

The research of HEAs over the past 16 years mainly focused on structural metallic materials by improving mechanical property including hardness, elasticity modulus, shearing modulus, strength of extension, and coefficient of thermal expansion.<sup>1,2,7–26</sup> Recently, novel applications of HEAs as functional materials have begun to draw attention from both theoretical and experimental perspectives, especially for heterogeneous catalysts.<sup>27–45</sup> In spite of limited reports on the study of HEA catalysis, HEA-based catalysts have exhibited remarkable catalytic performance in several thermal-driven and electrocatalytic reactions.<sup>27–45</sup> Compared with the research of

HEA-based catalysis that is just in its infancy, the understanding of bimetallic alloy catalysis achieves great progress with the development of nanoscience and nanotechnology. For electronic structures, the surface charge on bimetallic alloys will redistribute because of different work function of metals, while the *d*-band center of bimetallic alloys is able to be facilely tuned by varying the elemental composition.<sup>46–54</sup> The electronic properties of bimetallic alloys directly govern the adsorption and activation of reactants and intermediates and thereby determine the catalytic performance. For example, Au atoms with negative charges in AuPd alloys promote the activation of O<sub>2</sub> molecules by donating electrons to the antibonding orbital,<sup>55–57</sup> and the *d*-band center of Pt-based bimetallic alloys directly correlates to the adsorption energy of oxygen species in electrocatalysis.<sup>58–60</sup> When it comes to geometric structures, the arrangement of different metallic atoms on the surface of bimetallic alloys generates distinct active centers, which is also well-known as ensemble effect.<sup>61–64</sup> As a result, bimetallic alloys serve as superior heterogeneous catalysts for a number of reactions with enhanced activity, selectivity, and stability than their monometallic counterparts. Moreover, the introduction of non-noble metals into noble-metal catalysts also greatly reduces the cost of catalysts. For instance, the catalytic activity of Pt<sub>3</sub>Ni nanocrystals is far exceeding that of Pt nanocrystals toward oxygen reduction reaction (ORR).<sup>53,65–67</sup>

Relative to binary alloys, HEAs are composed of more components. The two elements of binary alloy often present a large immiscible gap with the generation of more stable phase-separated materials or intermetallic compound, which restricts the continuous regulation of the composition ratio and also the catalytic activity.<sup>27,28</sup> For HEAs, the larger configuration entropy induced by multiple compositional elements contributes to the formation of a stable single-phase solid solution structure rather than a fragile intermetallic compound.<sup>7,8,27,28</sup> Thus, HEAs not only regulate the electronic and geometric structures to a large degree but also serve as a platform to construct catalysts with unexpected performance.

HEA-based catalysts with improved catalytic activity is potentially able to be obtained by rationally tuning the composition and geometric structures of HEAs. The high entropy of HEAs breaks up the immiscible gap of elements, in favor of the robust control of element concentrations, and promotes the optimization of catalytic properties.<sup>27,28</sup> Inherent synergistic effect of HEAs enables boosting the catalytic activity via combining catalytically active metals.<sup>7</sup> Besides, with multiple elements, there are a huge number of possible atom arrangements on the surface of HEAs, inducing different adsorption modes of reactants and intermediates. Finely regulating the surface geometry of HEAs is theoretically capable of maximizing the adsorptive site for reactants as well as intermediates and efficiently activating reactants, leading to a desirable reaction rate.<sup>68,69</sup> Moreover, the severe lattice distortion due to the atomic size mismatch makes HEAs virtually in a thermodynamically nonequilibrium state. Hence, HEAs possess higher potential energy, resulting in a lower energy barrier during catalytic process.<sup>30</sup> Besides catalytic activity, the tunability of electronic structures of HEAs, such as *d*-band center, is beneficial for the enhancement of catalytic selectivity. The *d*-band center possesses a scaling relationship with the adsorption energy of reactants/intermediates. Generally, an upshift of the *d*-band center leads to a stronger metal–molecule interaction, whereas a downshift of the *d*-band center results in weaker binding.<sup>58,60</sup> The interaction between *d*-bands of constituent

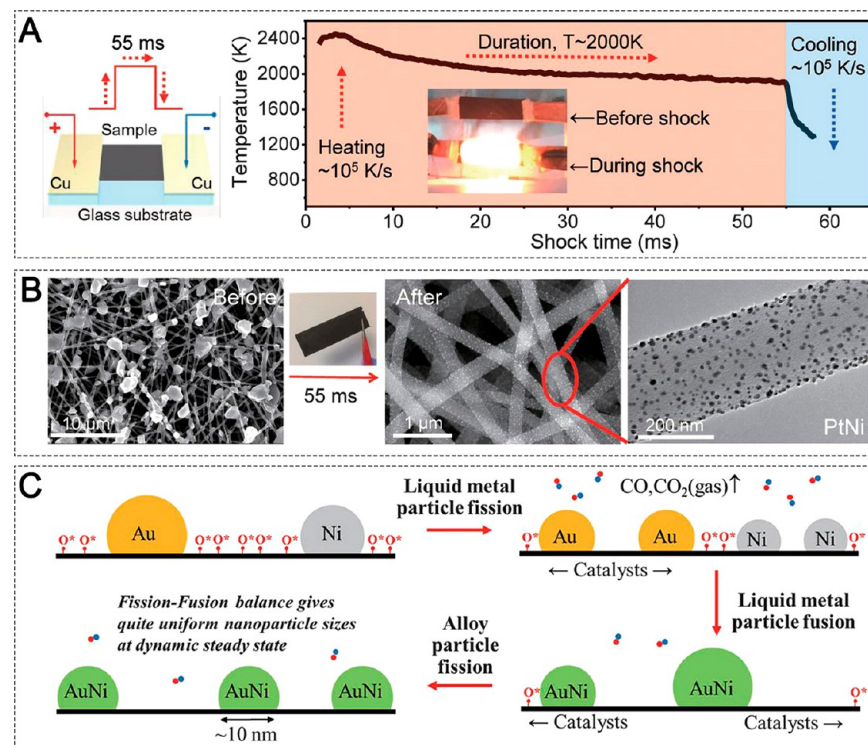


**Figure 2.** (A) Schematic illustration of CTS process for the preparation of HEA NPs. (B) The transformation of micro-sized precursor salt particles to well-dispersed HEA NPs after CTS. (C) An illustration of the catalysis-driven particle fission/fusion mechanism to synthesize uniformly dispersed HEA-NPs. (A–C) Reproduced with permission from ref 29. Copyright 2018 American Association for the Advancement of Science.

metals in HEAs assists to alter the position of *d*-band centers of active components, thus regulating the binding energy of key intermediates and further enhancing the electivity for expected product.<sup>58,60</sup> Strain induced by lattice distortion is also capable of changing the *d*-band center. A tensile lattice strain upshifts the *d*-band center, leading to a stronger interaction with adsorbates, while compressive strain downshifts the *d*-band center, thereby weakening the interaction.<sup>70,71</sup> What's more, charge redistribution on the surface, owing to the different work function for metal components, induces the alternative accumulation and scarcity of electrons across the whole surface of HEAs. The unique charge distribution is also able to affect the adsorption of reactants and enhance the product selectivity. From the aspect of catalytic stability, the high entropy and sluggish diffusion effect greatly enhance the thermal stability, further improving the durability of HEAs under various reaction conditions, such as high temperature, air conditions, acidic/alkaline environment, and so on.<sup>34</sup> Consequently, the inherent properties of HEAs are beneficial for the improvement of catalytic activity, selectivity, and stability via the regulation of geometric and electronic structures, making HEAs serve as a competitive candidate for the exploration of highly efficient catalysts.

Henceforth, in this Review, we focus on the recent research efforts, challenges, and opportunities related to HEA-based catalysis. As the fundamental aspect of this research area, the synthetic methods for HEA-based catalysts are first introduced and systematically compared. Classified by catalytic reactions, the catalytic performance as well as mechanistic understanding of HEA-based catalysis are inventoried and discussed. More importantly, the challenges and opportunities are proposed to show the future development directions in HEA-based catalysis based on the best of the authors' knowledge.

## 2. SYNTHETIC METHODS FOR HEA-BASED CATALYSTS

Facile and controlled synthesis of HEA-based catalysts is the foundation for the application of HEAs into heterogeneous catalysis. It is well acknowledged that only the atoms on the surface of catalysts directly participate in the catalytic reaction.<sup>72</sup> As a result, much different from the preparation method of HEA-based structural materials in meter scale, the synthesis of HEA-based catalysts requires a decrease in the size of HEAs down to nanoscale in order to increase specific surface areas. Wet-chemical methods are the most common synthetic methods for the preparation of bimetallic alloy nanocrystals as heterogeneous catalysts. Thanks to the efforts from a number of groups, the size, exposed facet, and compositions of bimetallic alloy nanocrystals have been precisely controlled.<sup>73–82</sup> Nevertheless, most studies via wet-chemical methods report the formation of nanocrystals with separated phases rather than alloys when the number of components exceeds three elements. Very recently, some breakthroughs in the synthesis of HEA-based catalysts have been achieved by applying nontraditional methods.<sup>27–33,35,38,39,42,45,102,114–116</sup>

**2.1. Carbonthermal Shock Synthesis.** Hu and his co-workers first proposed a general route for alloying up to eight dissimilar elements into HEA nanoparticles (NPs) on carbon nanofiber (CNF) supports by using carbonthermal shock (CTS) technology.<sup>27,29</sup> In brief, metal salt precursor  $MCl_xH_y$  ( $M = Pt, Pd, Ni, Fe, Co, Au, Cu, Sn$ , etc.) are mixed in a solution and loaded onto CNFs, followed by CTS. Taking the process of synthesizing PtNi alloy NPs as an example, the CNF support loaded by the precursors is connected to an electric pulse control device, and heated by flash heating ( $\sim 10^5$  K/s) to about 2000 K under Ar atmosphere. The sample is exposed to thermal shock for 55 ms, and then quickly cooled ( $\sim 10^5$  K/s) for 10 ms (Figure

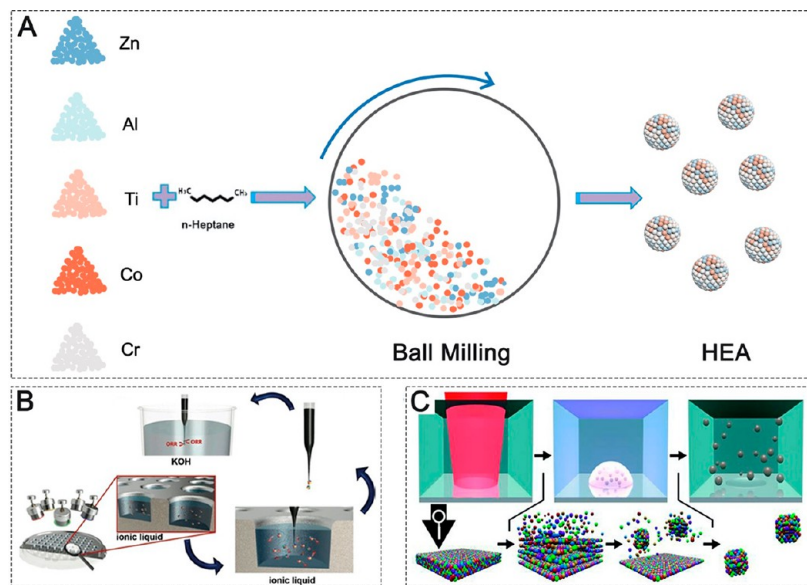
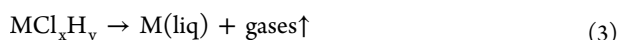


**Figure 3.** (A) Schematic illustration of mechanical alloying process for the synthesis of HEAs. (B) Strategy for the evaluation of HEA NPs by means of combinatorial cospattering into an ionic liquid. Reproduced with permission from ref 39. Copyright 2018 Wiley-VCH. (C) Qualitative representation of the laser-based synthesis of HEA NPs. Reproduced with permission from ref 38. Copyright 2019 Royal Society of Chemistry.

2A). Microsized precursor salt particles on the CNF support are transformed into NPs with uniform dispersion (Figure 2B). Besides binary PtNi NPs, more complex alloy NPs are also successfully prepared, such as binary FeNi and AuCu; ternary PtPdNi, AuCuSn, and FeCoNi; quinary PtCoNiFeCu and PtPdCoNiFe; senary PtCoNiFeCuAu; septenary PtPdCoNi-CuAu; and octonary PtPdCoNiFeCuAuSn NPs.<sup>29</sup>

About 2000 K of the operating condition far exceeds the thermal decomposition temperature of the metal salt precursors but is still lower than the boiling point of the metal element. The following reaction will occur during CTS:



The metal elements are anticipated in the liquid phase with the same size (micron order) as the original metal salt precursors. In addition, a synthetic mechanism was proposed by a catalytically driven carbon metabolism reaction:



where O\* denotes surface-bound residual oxygen. During the CTS, the liquid metal droplets actively travel around and split to harvest the dispersed O\* on the carbon surface. Mechanistically, a larger O\* concentration and the use of catalytically active metals are able to drive vigorous metabolism with more frequent catalyst motion and fission events (Figure 2C).<sup>83–86</sup> Taking the formation process of AuNi alloy as an example, large droplets (micron-sized) of Au and Ni are cracked into smaller droplets (nano level) by the catalytic driving force and will move intensely to uniformly mix small droplets of Au and Ni to obtain a single-phase solid solution. In the 55 ms of CTS process, the number of liquid metal aggregation and splitting is more than 10<sup>6</sup> times, which can completely achieve the uniform nanoscale dispersion and homogeneous high-entropy mixing of metal NPs.<sup>76,87,88</sup>

By facilely controlling the parameters of CTS, a variety of multicomponent NPs with required composition, size, and phase can be synthesized. (i) The concentration of surface defect on CNF supports controls the size and uniformity of HEA

NPs. The carbonization temperature of CNF supports directly governs the amount of surface defect (surface O\*). When CNF supports are carbonized at lower temperature, the residual amount of O\* will increase, contributing to the formation of HEA NPs with smaller size and better uniformity.<sup>29</sup> (ii) The duration of CTS also regulates the size and uniformity of HEA NPs. High-temperature exposure in the CTS process will reduce the amount of O\* on CNF supports, thereby inhibiting the fission and corresponding dispersity of metallic particles. As a result, smaller and more uniform HEA NPs are synthesized by shortening the duration of CTS.<sup>29</sup> (iii) The cooling rate adjusts the phase of formed NPs. HEA NPs are prepared at fast cooling rates, while Janus NPs are synthesized at low cooling rates because of solute partitioning. A cooling rate of about 10<sup>5</sup> K/s prevents the metallic solutes from being distributed over a distance of about 10 nm, thereby forming HEA structures.<sup>29,76,89</sup>

**2.2. Mechanical Alloying.** The mechanical alloying process is a simple and effective method to promote the formation of HEA powders by five or more components with mechanical force. Based on the calculation for the composition of HEA powders, pure metal powders are mixed with a certain proportion and put into a high-energy planetary ball miller together with a milling media (usually stainless steel balls). Under the strong collision and agitation of the steel balls, different metal powders undergo repeated cold welding, milling, and rewelding processes.<sup>90</sup> Under high-speed friction, repeated cold welding process induces the bonding of metal atoms between the contact surfaces of different metal powders.<sup>91,92</sup> In addition, smaller particles with lattice defects are constantly generated because of repeated impact and break during milling process.<sup>31</sup> At the same time, the generated local heating at the instant of the collision promotes the diffusion of lattice defects, contributing to the formation of interatomic bonds. As a consequence, HEA powders are able to be obtained by ball milling for a period of time (Figure 3A). Lv and his co-workers successfully synthesized AlCoCrTiZn, AlCoCrFeNi, and CoCrFeMnNi HEA powders through mechanical alloying.<sup>30</sup> Using pure metal powders with the size of ~40 μm as the

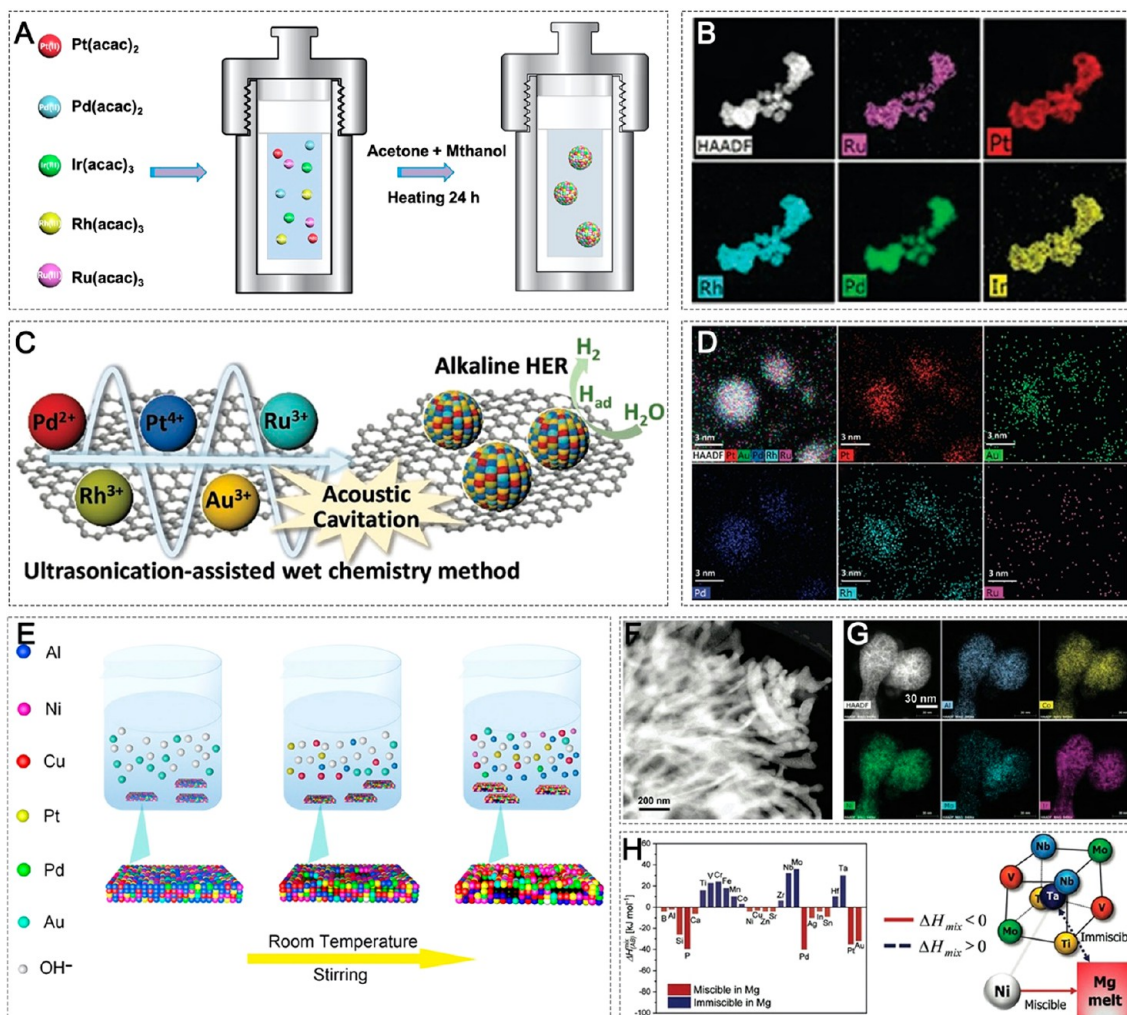


**Figure 4.** (A) Schematic illustration of solvothermal synthesis of HEAs. (B) The elemental mapping images of HEAs prepared by solvothermal synthesis.<sup>102</sup> (C) Schematic illustration of synthesis of HEAs/carbon catalysts by ultrasonication-assisted wet chemistry method.<sup>35</sup> (D) The elemental mapping images of HEAs prepared by ultrasonication-assisted wet chemistry method.<sup>35</sup> (E) Schematic diagram of dealloying method for the synthesis of HEAs. (F,G) Characterization of nanoporous HEAs.<sup>33</sup> (H) Enthalpy of mixing between the Mg melt and considered elements and predetermined liquid metal dealloying system based on the miscibility of precursor elements.<sup>114</sup> (B–D and F–H) Reproduced with permission from refs 33, 35, 102, and 114. Copyright 2019 Wiley-VCH.

precursor powders and *n*-heptane as the process inhibitor, HEA powders are facilely prepared under the protection of Ar atmosphere after ball milling for 60 h. These HEA powders are highly irregular in shape with the size of 0.5–10  $\mu\text{m}$ , while the surface of as-obtained powders is rough with a number of defects. Wu et al. also prepared AlFeMnTiCr, AlFeMnTiCo, and AlFeMnTiNi powders via a ball milling process by using pure metal powders as precursors and stearic acid as the process control agent.<sup>31</sup>

**2.3. Sputtering Deposition.** Sputtering deposition is a widely used technique to deposit NPs or thin films on substrates, which is also applied to fabricate HEA NPs.<sup>39,42,83–96</sup> Taking the preparation of  $\text{Pt}_{50}\text{Fe}_{11}\text{Co}_{10}\text{Ni}_{11}\text{Cu}_{10}\text{Ag}_8$  HEA NPs as an example, single-metal powders of Fe, Co, Ni, Cu, and Ag with high purity and fine grain size are mixed according the prescriptive molar ratio and then pressed under a pressure of 2500 psi to form a multielement alloy target. The multielement alloy target is further pressed together with a high-purity thin Pt sheet to obtain  $\text{Pt}_{50}\text{Fe}_{11}\text{Co}_{10}\text{Ni}_{11}\text{Cu}_{10}\text{Ag}_{10}$  alloy target. The metal atoms in the target are sputtered by Ar plasma, and deposited on the substrate to form HEA NPs. With the

extension of the deposition time, the HEA NPs grow up uniformly on the surface of the substrate. It is worth noting that the composition of as-obtained HEA NPs is quite close to that of the original alloy target, indicating that each element is sputtered indiscriminately and deposited on the substrate. Thus, the composition of HEA NPs could be simply controlled by tuning the corresponding composition of the target.<sup>42</sup>

Recently, Schuhmann and his co-workers improved the sputtering deposition technique to synthesize highly dispersed HEA NPs.<sup>39</sup> They bombarded the element target with Ar plasma and sputtered the metal atoms in the target into the ionic liquid rather than the substrates. These metallic atoms will then nucleate and grow in the ionic liquid to generate the corresponding HEA NPs (Figure 3B). In addition, the elemental composition of HEA NPs can be altered by adjusting the speed of sputtering deposition. Acting as the stabilizing and suspension medium, the ionic liquid also affects the size of HEA NPs. A series of CrMnFeCoNi HEA NPs is synthesized by cosputtering the metal atoms in the element target into the ionic liquid.

**2.4. Kinetically-Controlled Laser Synthesis.** Kinetically controlled laser synthesis is a novel route to fabricate HEA

nano particle with excellent reproducibility and scalability.<sup>38,97,98</sup> To synthesize equimolar CoCrFeNiMn HEA NPs, an equimolar ablation target is first prepared by mixing, pressing, and heating single-metal powders in sequence. The ultrafine picosecond pulsed laser is irradiated on the surface of the ablation target in ethanol solution, so that a large number of metallic atoms are excited and plumes are also formed by atomization and ionization. In addition, cavitation bubbles are simultaneously formed at the solid–liquid interface. Inside the cavitation bubbles, metallic atoms, ions, and clusters will undergo the process of nucleation and condensation to grow into stable HEA NPs. With the rupture of the cavitation bubbles, these HEA NPs are released and electrostatically stabilized in ethanol solution (Figure 3C). The hydrodynamic diameter of most of HEA NPs is 2.8 nm, indicating that laser synthesis method is able to obtain a large number of isolated ultrafine NPs due to fast kinetics.<sup>99,100</sup> In addition, larger NPs are also produced in a highly dynamic molten layer on the surface of the ablation target because of Taylor-Rayleigh instability.<sup>101</sup> In terms of compositions and crystalline structures, HEA NPs mainly retain the properties of the original ablation target. As a bonus, up to 3 g of HEA NPs is prepared per hour by kinetically controlled laser synthesis. The remarkable scalability is highly attractive for potential application of HEA NPs as heterogeneous catalysts in chemical industry production and environmental protection. Furthermore, eco-friendly and economical water is able to be also used as the ablation fluid instead of ethanol, which exhibits an even higher ablation rate.<sup>38</sup>

**2.5. Solvothermal Synthesis.** The Iversen group proposed a simple and universal method to synthesize HEA NPs by solvothermal synthesis.<sup>102</sup> Solvothermal synthesis is developed on the basis of hydrothermal synthesis, allowing a chemical reaction taking place in a nonaqueous solvent at temperature above the boiling point and pressures above 1 bar.<sup>102,103</sup> By using noble-metal acetylacetone as the precursors and an acetone-ethanol mixture as the solvent, bimetallic  $Pd_xRu_{1-x}$ ,  $Pt_xRu_{1-x}$ ,  $Ir_xRu_{1-x}$ ,  $Rh_xRu_{1-x}$ ,  $Ir_{1-x}Pt_x$ , and  $Rh_{1-x}Pt_x$  alloy NPs are successfully obtained via a low-temperature solvothermal autoclave synthesis at 200 °C for 4–24 h. Impressively, the composition of bimetallic alloy NPs could be altered across the entire composition range with face-centered-cubic (fcc) crystalline structures. Furthermore, quaternary and quinary HEA NPs are also prepared by simply tuning the precursors in the process of solvothermal synthesis (Figure 4A,B). The use of acetylacetones is the key point to the fabrication of HEA NPs. The strong metal-acetylacetone interaction facilitates coprecipitation by slowing down the rate of the precipitation. Generally, the most stable crystalline structure for metallic Ru is hexagonal close packed (hcp) structure. For Ru-based alloy NPs (bimetallic and HEA NPs), fcc structures are observed across wide composition range.<sup>104–107</sup> Metal acetylacetones are highly suited for the synthesis of single-phase NPs. In addition, the regulation of crystalline structures of HEA NPs also opens up a new avenue to promoting catalytic performance.

**2.6. Ultrasonication-Assisted Wet Chemistry.** By wet chemistry method, alloy NPs are formed by the reduction of metallic precursors in solution at the heating temperature below 300 °C. The generation of alloy NPs is mainly driven by enthalpy interactions among metallic species, which also limits the synthesis of HEA NPs by traditional wet chemistry methods.<sup>108,109</sup> Liu et al. reported a facile ultrasonication-assisted wet chemistry method for preparing HEA NPs (Figure 4C).<sup>35</sup> In an ultrasound irradiation process, extremely high

temperatures in localized microscopic regions at momentary timespans are derived from the acoustic cavitation phenomenon. Up to ~5000 °C of temperature and ~2000 atm of pressure are generated in localized microscopic regions at a time scale of less than 10<sup>-9</sup> s, directly accelerating the simultaneous reduction of metallic ions to form entropy-maximized state.<sup>110,111</sup> In synthetic process, ethylene glycol is selected as both the solvent and reducing agent. PtAuPdRhRu HEA NPs with the size of ~3 nm on carbon supports are prepared via ultrasonic process in ethylene glycol solution at room temperature (Figure 4D). It is worth noting that the stability and crystalline purity of formed PtAuPdRhRu HEA NPs is able to be further improved by calcination at 700 °C under N<sub>2</sub> atmosphere without changing the size of HEA NPs.

**2.7. Dealloying Method.** Serving as efficient catalysts, nanoporous metals are generally prepared by wet etching process. A notable example is the preparation of nanoporous Au from AuAg alloy by a electrochemical dealloying process.<sup>112,113</sup> This synthetic strategy could also be applied in the construction of HEA nanomaterials with porous structures. Qiu and his co-workers successfully designed and prepared a series of nanoporous HEAs, including AlNiCuPtPdAu, AlNiCuPtPdAu-CoFe, and AlNiCuMoCoFe.<sup>32</sup> Taking the process of synthesizing senary AlNiCuPtPdAu HEA as an example, Al<sub>97.5</sub>Ni<sub>0.5</sub>Cu<sub>0.5</sub>Pt<sub>0.5</sub>Pd<sub>0.5</sub>Au<sub>0.5</sub> precursor alloy is prepared by melting pure metals using an induction-melting furnace under Ar protection, followed by spinning to form the alloy ribbons. The metallic Al element is selectively etched into Al ions in NaOH aqueous solution, leading to the formation of nanoporous HEAs with a ligament size of ~3 nm (Figure 4E). Caused by the atomic diffusion on the surface, the coarsening phenomenon usually occurs in nanoporous metals with alloy ligaments. In the synthesis of nanoporous HEAs, a tremendous increase of the structural entropy enhances the stability of crystalline phase. The low diffusion rate of Pt element also suppresses the diffusion of Au and Cu elements, promoting the stability of HEAs as well as downsizing the nanoporous structure. Noticeably, it is difficult to etch all Al element in nanoporous HEAs. The as-obtained nanoporous HEAs all inevitably contain Al element. Ir-based nanoporous HEAs are also synthesized by Qiu et al. via a similar dealloying method (Figure 4F,G).<sup>33</sup> Joo et al. improved the dealloying method by proposing liquid metal dealloying instead of etching distinct metallic element in an alkaline solution, which prevents the oxidation of metals during the dealloying process.<sup>114</sup> Metallic Ti, V, Nb, Mo, and Ta cannot be fused with metallic Mg, while metallic Ni is able to be melted in metallic Mg (Figure 4H). Nanoporous TiVNbMoTa HEA is constructed by removing the Ni element from (TiVNbMoTa)<sub>25</sub>Ni<sub>75</sub> precursor alloy in the Mg melt.

**2.8. Fast Moving Bed Pyrolysis (FMBP) Method.** With higher specific surface area, enhanced surface energy, and interface effect, supported NPs (NPs) often exhibit enhanced catalytic activity and stability than NPs themselves. Moreover, NPs are usually dispersedly immobilized on granular supports for industrial applications, such as Al<sub>2</sub>O<sub>3</sub>, zeolite, carbon materials, and so on. Loading HEA NPs on supports is a promising strategy for the application of HEA in catalysis, but it suffers from the problems of uneven dispersion and favor of aggregation.<sup>115</sup> Recently, Lu et al. designed a general and facile FMBP method following wet impregnation, successfully preparing ultrasmall and homogeneous HEA NPs loaded on various supports (Figure 5A).<sup>35</sup> Compared with fixed bed

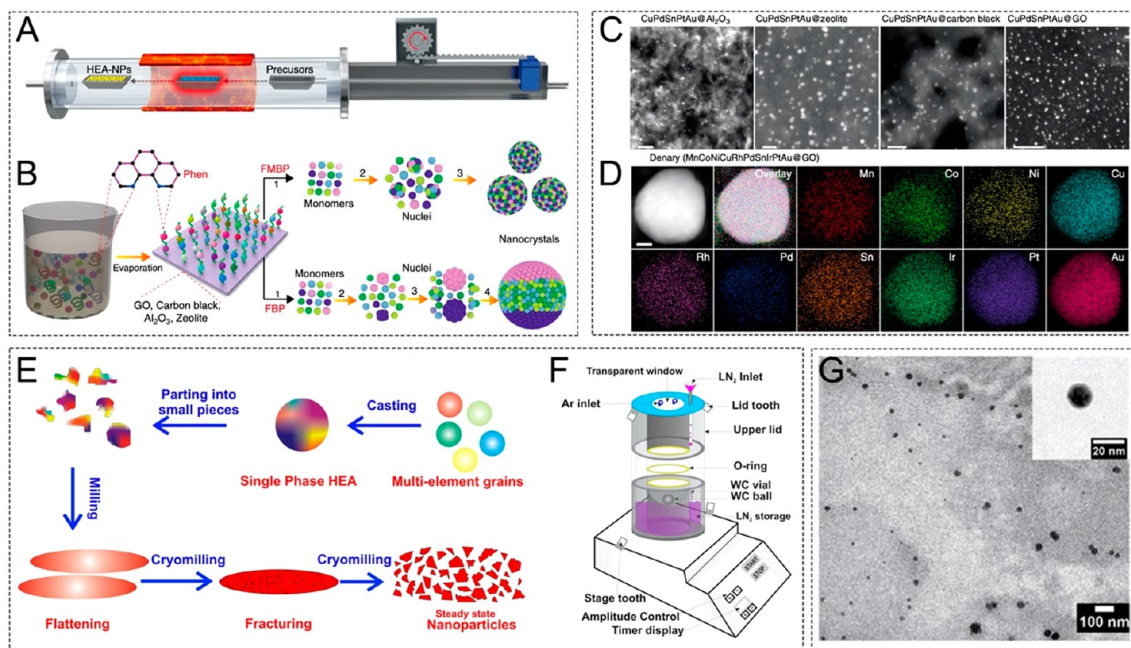


**Figure 5.** (A) Schematic illustration of the FMBP experimental setup for the synthesis of HEA NPs. (B) Schematic illustrations for synthesis of homogeneous and phase-separated HEA NPs by FMBP and FBP methods, respectively. (C) STEM images revealed that the HEA-NPs synthesized by the FMBP strategy were highly dispersed on  $\gamma$ -Al<sub>2</sub>O<sub>3</sub>, zeolite, carbon black, and GO. All scale bars represent 20 nm. (D) HAADF-STEM and EDX elemental maps of denary MnCoNiCuRhPdSnIrPtAu HEA and supported on GO. The scale bar represents 10 nm.<sup>115</sup> (A–D) Reproduced with permission from ref 115. Copyright 2020 Springer Nature. Schematic diagrams of (E) the formation process of HEAs NPs in cryomilling, and (F) custom-built single-ball cryomill (WC-Tungsten carbide). (E,F) Reproduced with permission from ref 116. Copyright 2018 Springer Nature. (G) TEM image of AuAgPtPdCu HEA NPs; the inset shows a high-magnification image of a single nanoparticle. Reproduced with permission from ref 45. Copyright 2020 American Chemical Society.

**Table 1. Summary of Different Synthetic Methods for HEA-Based Catalysts**

synthetic method	equipment	temperature and pressure	size	size uniformity	element applicability	substrate applicability	productivity
carbonthermal shock synthesis	current pulse device	~2000 K/1 atm	3–25 nm	good	NM <sup>a</sup> : Au, Pt, Pd, Ru, Rh; NN <sup>b</sup> : Fe, Co, Ni, Cu, Mo, Sn, Ce	only carbon support	~100 mg
mechanical alloying	planetary ball mill	RT <sup>c</sup> /1 atm	0.5–20 $\mu$ m	poor	NM: Ag, Pt, Pd, Ru, Rh; NN: Cr, Co, Ni, Cu, Mo, Sn, Ce	free-standing	~20 g
sputtering deposition	UHV deposition system	RT/ultrahigh vacuum	1–4 nm	good	NM: Ag, Pt; NNM: Co, Cr, Fe, Mn, Ni	suitable for various supports	~200 mg
kinetically controlled laser	pulsed laser	RT/1 atm	2–5 nm	good	NN: Fe, Co, Ni, Cu, Cr	suitable for various supports	3 g/h
solvothermal synthesis	hydrothermal reactor	200 °C/1 atm	1–100 nm	medium	NM: Pt, Pd, Ru, Rh, Ir;	suitable for various supports	~10 mg
ultrasonication-assisted wet chemistry	ultrasonication processor	RT/1 atm	2–80 nm	good	NM: Au, Pt, Pd, Ru, Rh	suitable for various supports	~100 mg
dealloying method	smelting furnace/ Spinning machine	500 °C/1 atm	pore-size: ~2–3 nm	good	NM: Au, Pt, Pd, Ir; NN: Al, Fe, Co, Ni, Cu, Cr, Nb, V, Ta	free-standing	~10 g
fast moving bed pyrolysis method	tube furnace	923 K/Ar	5–50 nm	good	NM: Rh, Pd, Ir, Pt, Au; NN: Mn, Co, Ni, Cu, Sn	suitable for various supports	~100 mg
cast cum cryo-milling method	cryomill	160 ± 10 °C /Ar	3–14 nm	good	NM: Ag, Au, Pt, Pd, NN: Fe, Cr, Mn, Ni, Co, Cu, V, Al,	free standing	~10 g

<sup>a</sup>NM: Noble metal. <sup>b</sup>NN: Non-noble metal. <sup>c</sup>RT: Room temperature.

pyrolysis (FBP) reactor, the FMBP method achieves the simultaneous pyrolysis of the mixed metal precursors owing to the rapid heating rate, resulting in the formation of smaller nuclei clusters to form HEA NPs without phase separation (Figure 5B). Take the synthesis of CuPdSnPtAu HEA NPs supported on graphene oxide (GO) as an example. First, GO is suspended into the mixed solution of ultrapure water and alcohol by an ultrasound for 12 h at 318 K. Then, metal chloride precursors are added into the GO solution at an interval of 15 min in the order of the metal activity in order to avoid the direct reduction of active metal, followed by being evaporated to dryness at 323 K in

the ultrasound system. A quartz boat with the as-obtained metal precursors loading on GO is pushed into the hot zone when the furnace temperature is increased to 923 K under Ar atmosphere. The mixture anneals for 2 h at 923 K to ensure the simultaneous pyrolysis of the mixed metal precursors. After they were allowed to cool naturally to room temperature, CuPdSnPtAu HEA NPs supported on GO (CuPdSnPtAu@ GO) with an average size of ~50 nm are obtained (Figure 5C). A wide range of HEA NPs with up to 10 elements uniformly immobilized on other supports are successfully fabricated following similar procedure, such as CuPdSnPtAu@Al<sub>2</sub>O<sub>3</sub>, CuPdSnPtAu@carbon black, CuPdSnP-

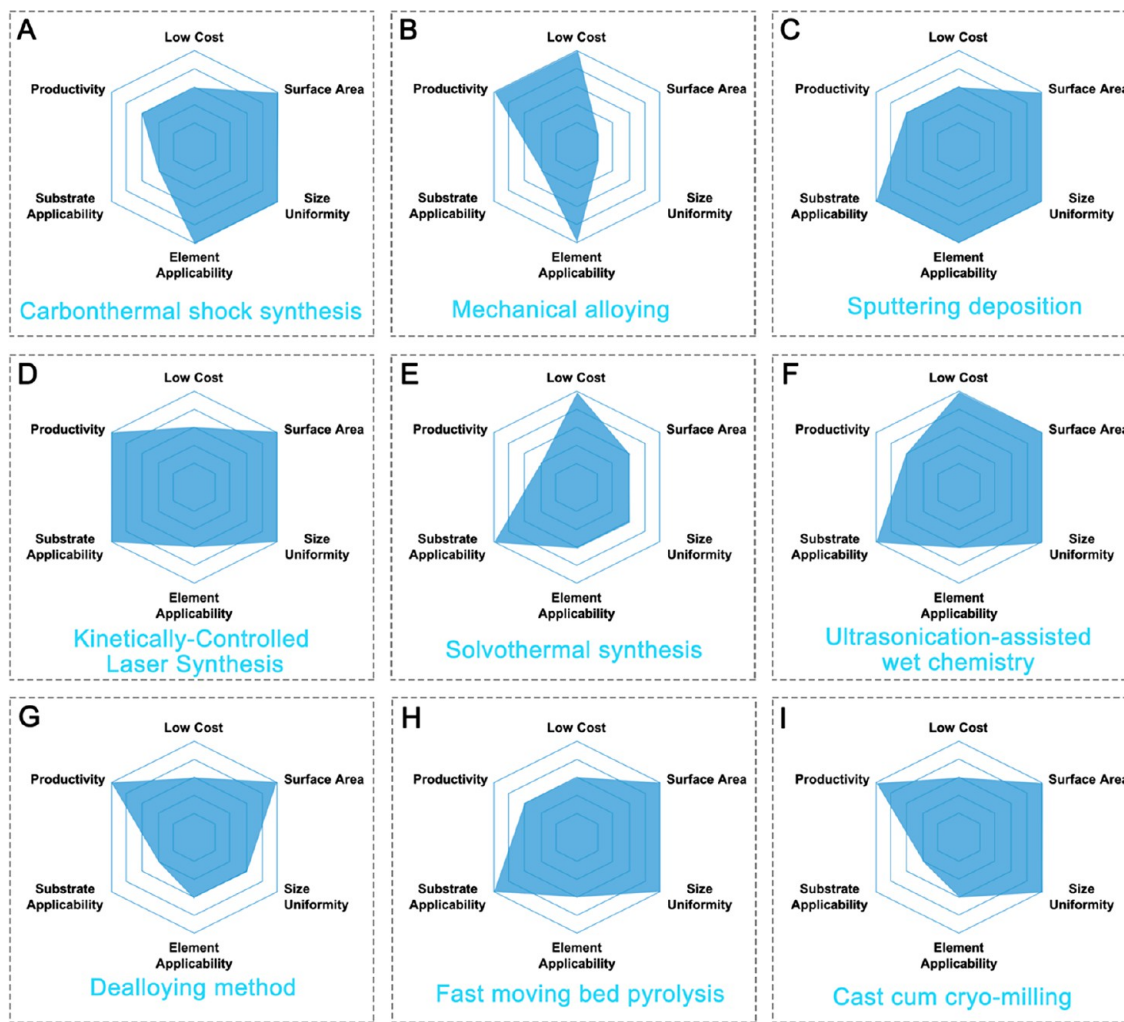


**Figure 6.** Comparison of different synthetic methods for HEAs in terms of cost, surface area, size uniformity, elemental applicability, substrate applicability, and productivity.

tAu@zeolite, denary MnCoNiCuRhPdSnIrPtAu@GO, and so on (Figure 5C,D). It is worth noting that when  $\gamma$ -Al<sub>2</sub>O<sub>3</sub> or zeolite is used as supports, H<sub>2</sub> is required for the reduction of metal precursors under 923 K.

**2.9. Cast cum Cryo-milling Method.** Though conventional mechanical alloying process is a facile method to prepare HEA, it often requires longer milling times. Furthermore, the size and surface morphology of HEA via this method is difficult to control due to contamination and phase change. Biswas and co-workers proposed a new casting followed by cryo-milling method for the fabrication of HEA NPs with few contaminations and narrow size distribution.<sup>116</sup> Generally, based on the composition and concentration of elements for HEA, corresponding metal powders are first melted under Ar environment to synthesize cast HEAs. The ingot is parted in smaller pieces and milled in a custom-built cryomill for a certain hour, after which HEAs are obtained (Figure 5E). The cryomill is a vibratory mill that has a single ball with a diameter of 5 cm and a 9.5 cm vial with volume of 250 cc. Thus, a 2 mm ball amplitude is maintained by using a tungsten carbide (WC) ball-vial (Figure 5F). The milling chamber is continuously purged by Ar gas to inhibit the oxidation of powder during milling. Quinary equimolar FeCrMnNiCo, CuAgAuPtPd, and FeCrMnVAl HEA NPs are successfully prepared, with an average size of 4, 9, and 6 nm, respectively.<sup>116</sup> Recently, Biswas et al. fabricated

AuAgPdPtCu HEAs via this method. Cast HEA ingot fabricated by melting Au, Ag, Pd, Pt, and Cu powders is milled in a cryomill for 6 h, and then AuAgPdPtCu HEA NPs with an average size of  $16 \pm 10$  nm are obtained (Figure 5G).<sup>45</sup>

**2.10. Comparison of Different Synthetic Methods.** We further systematically compare the advantageous and disadvantageous of these synthetic methods. As shown in Table 1, the required synthetic equipment, the required synthetic temperature and pressure, the size of HEAs, the size uniformity of HEAs, the applicability of metallic elements, the applicability of supports, and the productivity of HEAs for different synthetic methods are carefully listed. The equipment and synthetic conditions determine the cost of formed HEAs. Thus, Cost, surface area, size uniformity, element applicability, substrate applicability, and productivity are considered to assess different synthesis methods in this Review from the aspects of catalytic performance and practical application. (i) *Catalytic activity.* Surface area, element applicability and substrate applicability are selected in terms of catalytic activity.<sup>72</sup> Catalytic process mainly takes place on the surface of solid catalysts, thus a larger surface area provides more potential active centers and further enhances the catalytic performance.<sup>72</sup> As for element applicability, noble metals like Pt, Ir, and Ru with outstanding catalytic activity are still widely applied in various reactions, such as water splitting, oxygen reduction reaction, and methanol oxidation reaction,

whereas Cu is the most attractive metal for CO<sub>2</sub> reduction reaction.<sup>33,36,43,45</sup> Synthetic methods suitable for active metals for various reactions serve as powerful tools for the fabrication of efficient HAE-based catalysts, affecting the universality of synthetic procedures. Besides, loading particles onto substrates is a common strategy to improve catalytic activity because of the interaction between them, such as the formation of interface, Mott-Shottky barrier, and so on.<sup>58,117</sup> Thus, synthetic methods that are able to provide substrates for HEAs potentially contribute to the promotion of catalytic activity. (ii) *Catalytic selectivity.* Size uniformity is related with catalytic selectivity owing to the size effect of catalysts. The local geometric and electronic structures are significantly affected by the size of particles, which alter the adsorption configurations of reactant or intermediates and further the catalytic selectivity.<sup>118</sup> Preparing HEA with high size uniformity helps to achieve controllable synthesis of HEA and the fine-regulation of catalytic selectivity. (iii) *Catalytic stability.* Substrate applicability is also selected for the consideration of catalytic stability. Substrates have been reported to stabilize particles through defects and charge transfer.<sup>28,119</sup> Thus, synthetic methods suitable for various substrates potentially enhance the stability of HEAs. (iv) *Practical application.* Cost and productivity are associated with the practical application of the synthesis method. Lower cost and higher productivity contribute to the large-scale synthesis of HEA and meet the request of industrialized application.

Figure 6 shows the comparison of different synthetic methods for HEAs in terms of cost, surface area, size uniformity, elemental applicability, substrate applicability, and productivity. The CTS method is a novel route to fabricate HEA NPs with controllable composition, ultrafine size as well as narrow size distribution and is available for various elements. Nevertheless, the applicability of substrate is extremely hard to ameliorate for the CTS method because carbon supports are necessarily required in the synthetic process, and the production of this method is only in milligram scale. Fortunately, most industrially metallic catalysts are also loaded on carbon supports. If the productivity of HEAs via CTS technology could be greatly enhanced, this synthetic method will significantly promote the usage of HEA-based catalysts in industry. Mechanical alloying serves as a good method for synthesizing HEAs at low cost and large scale via a simple ball milling process, but the size uniformity and surface morphologies of HEAs prepared by this method are hard to control. Sputtering deposition is able to finely regulate the size of HEAs. Besides, this method is suitable for various substrates, contributing to the construction of supported HEAs. The disadvantage of sputter deposition is that it needs deposition equipment and ultrahigh vacuum conditions, which enhances the cost. Kinetically controlled laser synthesis is capable of obtaining ultrafine HEA NPs with excellent reproducibility and productivity. Nonetheless, kinetically controlled laser synthesis needs original ablation targets, where the immiscibility of elements may restrict the element applicability of this method. Solvothermal synthesis is a facile method to fabricate HEAs by using commercial metal precursors. Besides, a different substrate is able to be applied into HEAs via this method by adding a corresponding precursor for the substrates. However, solvothermal synthesis suffers from low productivity, and the size uniformity of HEAs prepared via this method needs further improvement. HEAs loaded on various substrates are also able to be gained by the ultrasonication-assisted wet chemistry method via an ultrasound irradiation process at room conditions. The dealloying method is suitable for fabricating porous HEAs with

enhanced surface areas and uniform pore structures. Moreover, the mass production of the dealloying method is able to reach gram or even kilogram scale, which is more suitable for industrial application. Nevertheless, the casting process for the preparation of precursor alloy needs high temperature and inert atmosphere, inducing a higher cost. *Fast moving bed pyrolysis (FMBP)* serves as an efficient strategy to load HEA NPs on various substrates, such as  $\gamma$ -Al<sub>2</sub>O<sub>3</sub>, carbon materials, zeolite, and so on. The fabricated HEA NPs are ultrasmall and homogeneously distributed on these supports. However, the FMBP method is equipment-demanding owing to the high temperature condition as well as a rapid heating rate. *Cast cum cryo-milling* is available for large-scale synthesis of HEAs with narrow size distributions, but HEAs prepared by this cast cum cryo-milling method are usually free-standing. In addition, the cryo-milling process needs specialized equipment.

**2.11. Key Characteristic Methods for HEAs.** HEAs exhibit great potential in the application of catalysis, which requires various characterization methods for assessing the properties of HEAs, including element compositions, microstructure and morphologies, crystallographic properties, and chemical states.

*Element Compositions.* Element compositions mainly include the element types, element distribution, and element concentrations. HEAs are usually composed of more than four elements, and the determination of element compositions is of great importance. Inductively coupled plasma-optical emission spectrometry (ICP-OES) and inductively coupled plasma-mass spectroscopy (ICP-MS) are widely employed to determine the composition of elements. It is worth noting that ICP-OES and ICP-MS usually provide composition information for the bulk of the sample and average over the whole catalyst.<sup>27,28,120</sup> Energy dispersive X-ray spectroscopy (EDX), which is often associated with electron microscopy, is a widely utilized technique for elemental analysis in a selected area. Linear scanning EDX spectrum is utilized to determine the atomic ratio of compositional elements by corresponding peak areas.<sup>120</sup> Moreover, EDX is also able to obtain spatially resolved elemental mapping that illustrates the element distribution. For HEA, higher entropy of HEAs accelerates the alloying process and contributes to the formation of uniform phase; thus, the elements of HEAs are often homogeneously distributed without elemental segregation or phase separation.<sup>27–45</sup> X-ray photoelectron spectroscopy (XPS) is another tool available for estimating the chemical composition with the integrated peak area of different elements, which is more sensitive to the surface region.<sup>27,120</sup> Combining these methods to detect the element compositions makes the results more accurate and reliable.

*Microstructure and Morphologies.* Scanning electron microscopy (SEM), transmission electron microscopy (TEM), and high-angle annular dark-field scanning transmission electron microscopy (HAADF-STEM) are all commonly used for the structural characterization of catalysts. These methods display HEAs' size, size distribution, surface morphology, exposed facets, and so on. For porous HEAs, Brunauer–Emmett–Teller (BET) and Barrett–Joyner–Halenda (BJH) measurements are needed to determine the specific surface area and pore volume as well as pore size distribution.<sup>120</sup>

*Crystallographic Properties.* X-ray diffraction (XRD) analysis is a powerful tool to determine the phase composition of HEA via peak positions and intensities.<sup>28,120</sup> At present, HEAs applied in catalytic field mainly possess single phase and a minority of them exhibit dual phases. The XRD profiles of

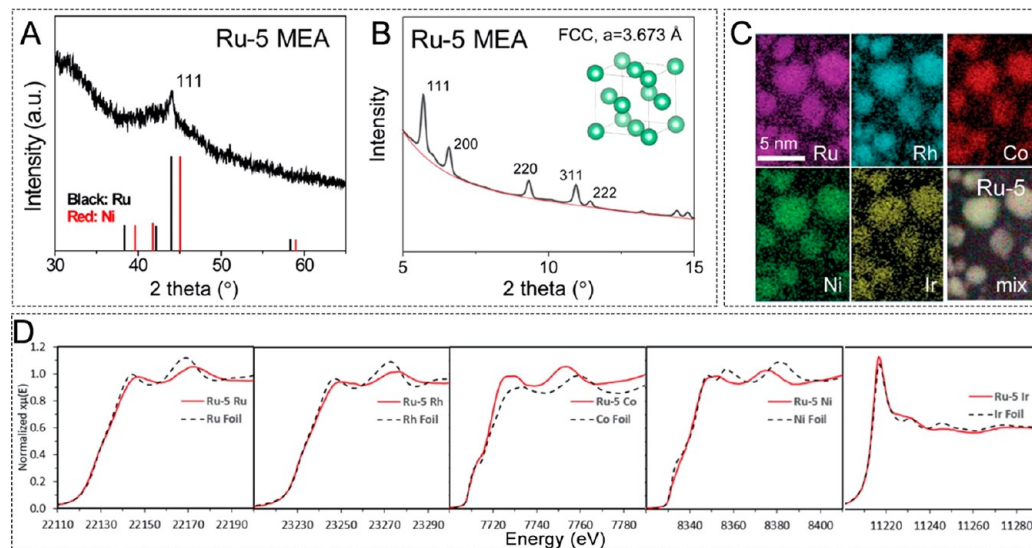


**Figure 7.** (A) Powder XRD profile, (B) synchrotron XRD profile, and (C) EDX elemental maps of RuRhCoNiIr HEA NPs. (D) XANES spectra of each element in RuRhCoNiIr HEA NPs. (A–D) Reproduced with permission from ref 28. Copyright 2020 American Association for the Advancement of Science.

single-phase HEAs often display only a set of diffraction patterns of fcc, bcc, hcp and so on, while HEAs with biphasic or even more phases exhibit additional diffraction peaks in XRD patterns.<sup>27–45</sup> Additionally, atomic-scale HAADF-STEM and corresponding fast Fourier transform (FFT) analysis also assist to identify lattice planes and further the crystal structure of HEAs.<sup>28</sup>

**Chemical States.** Chemical states, such as oxidation states and local coordination environments, have significant influence on the catalytic activity of HEAs. XPS is a popular measurement to determine the surface chemical properties of elements by mainly detecting the kinetic energy of photoelectrons emitted from surface atoms.<sup>120</sup> For HEAs, the surface elements are in metallic states in most cases. Noticeably, the surface elements of HEAs are sometimes oxidized and form an oxide coating on the surface of HEAs, which has been reported to promote catalytic activity and stability.<sup>32,37</sup> X-ray absorption spectroscopy (XAS) is usually applied to further confirm the chemical states of HEAs, including X-ray absorption near-edge structure (XANES) and extended X-ray absorption spectroscopy fine structure (EXAFS).<sup>120</sup> Compared with XPS, XANES provides information on the valence state of elements in bulk. XANES profiles generally indicate that the compositional elements of HEA are in metallic states.<sup>28</sup> EXAFS is often employed for the study of coordination and chemical-bonding properties, including coordination atoms, coordination number and bond length.<sup>120</sup> With multiple elements, the number of derived metal–metal bond type in HEAs is much higher and the local coordination environments are more complicated in HEAs relative to that of binary alloys.<sup>28</sup>

For the characterization of HEAs, numerous methods are applied and comprehensive analysis of the obtained results are required to ascertain the properties of HEAs. Take the determination of alloy structure of RuRhCoNiIr HEA as an example.<sup>28</sup> Powder XRD profile with a single peak preliminarily indicates single-phase alloy structure for RuRhCoNiIr HEA (Figure 7A).<sup>28</sup> The synchrotron XRD profile ( $\lambda = 0.2113 \text{ \AA}$ ) RuRhCoNiIr HEA further shows a clear single-phase fcc structure with a fitted lattice constant of  $3.673 \text{ \AA}$ , confirming the single-phase alloy formation (Figure 7B).<sup>28</sup> The microscopic

EDX elemental map illustrates each element is uniformly distributed without elemental segregation or the formation of immiscible phase, further demonstrating the formation of single phase (Figure 7C).<sup>28</sup> In addition, the slight deviation in the shape and intensity of the postedge features of the XANES spectrum further indicate the formation of alloy rather than elemental segregation into pure/unary metals (Figure 7D).<sup>28</sup> These above results together demonstrate the successful alloying process of RuRhCoNiIr at the nanoparticle level.

### 3. CATALYSIS OF HEAS

At present, there are several reports on the application of HEAs as heterogeneous catalysts in thermal-driven and electrocatalytic reactions. HEAs exhibit enhanced catalytic activity, selectivity, and stability relative to their monometallic and phase-separated counterparts. Serving as a discovery and platform to construct highly efficient catalysts with unexpected performance, HEAs have attracted increasing attention.

**3.1. Ammonia Decomposition Reaction.** Ammonia ( $\text{NH}_3$ ) is an important kind of industrial raw material to produce fertilizers and also is regarded as an excellent hydrogen storage carrier. As ammonia is able to be readily liquefied at a mild pressure of  $\sim 8$  bar at room temperature, catalytic decomposition of ammonia into hydrogen ( $\text{H}_2$ ) has attracted increasing attention.<sup>121</sup> Although noble-metal Ru nanocrystals are proven as the most active catalysts for the decomposition of  $\text{NH}_3$ , the high cost and scarcity have severely constrained their large-scale application.<sup>122</sup> Low-cost Co–Mo alloy nanocrystals are competitive candidates for  $\text{NH}_3$  decomposition based on the theoretical calculation of the adsorption properties of mixed sites on the alloy surfaces.<sup>123</sup> Nevertheless, the regulation of the composition ratio and further the catalytic activity of Co–Mo alloy is restricted by the large miscibility gap with the generation of more stable phase-separated materials or intermetallic compound.<sup>27,124</sup> Increasing the number of elements to construct HEA serves as a promising method to overcome this hurdle because the enhanced entropy can induce single-phase stabilization. The Wang group successfully applied HEA NPs to break up the miscibility limitation in the phase diagram

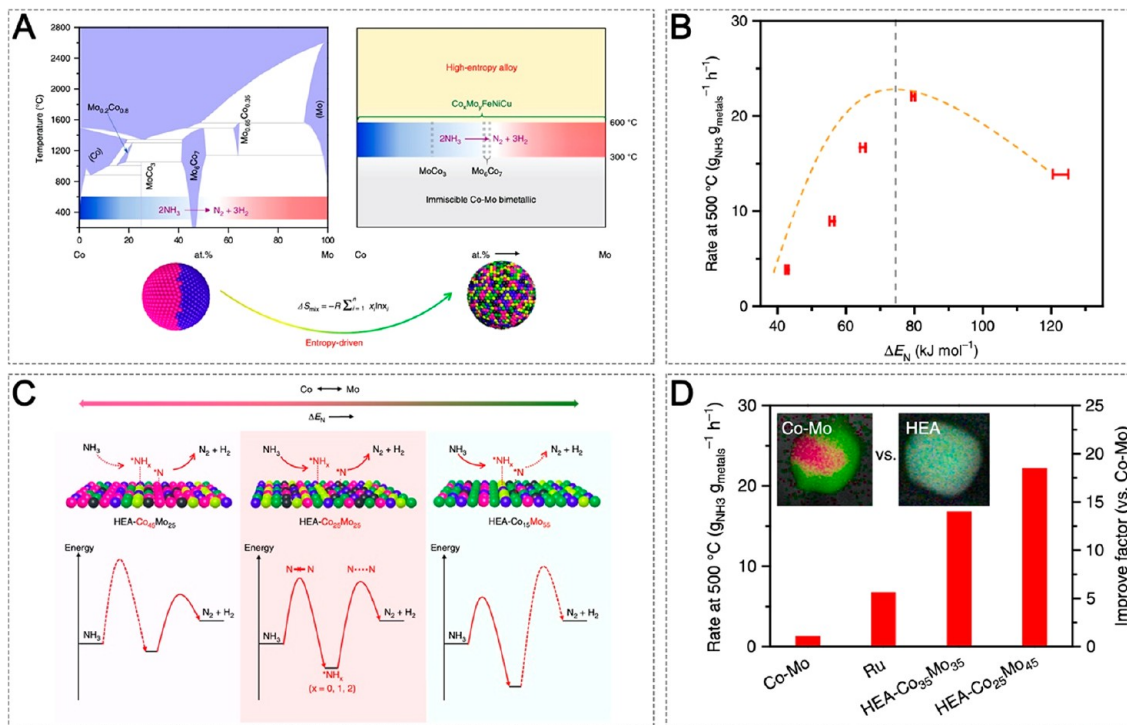


**Figure 8.** (A) HEA catalysts breaking the miscibility limitation of conventional binary alloys. (B) Correlations between the binding strength of nitrogen and catalytic activities. (C) Schematic illustration of the rate-limiting factors in  $\text{NH}_3$  decomposition. (D) Comparison of reaction rates measured in the kinetic regime among bimetallic Co–Mo, Ru, and HEA-Co<sub>x</sub>Mo<sub>y</sub> catalysts ( $T = 500$  °C). Inset: element maps for the bimetallic Co–Mo (Co/Mo = 25/45) and HEA-Co<sub>25</sub>Mo<sub>45</sub> catalysts. (A–D) Reproduced with permission from ref 27. Copyright 2019 Springer Nature.

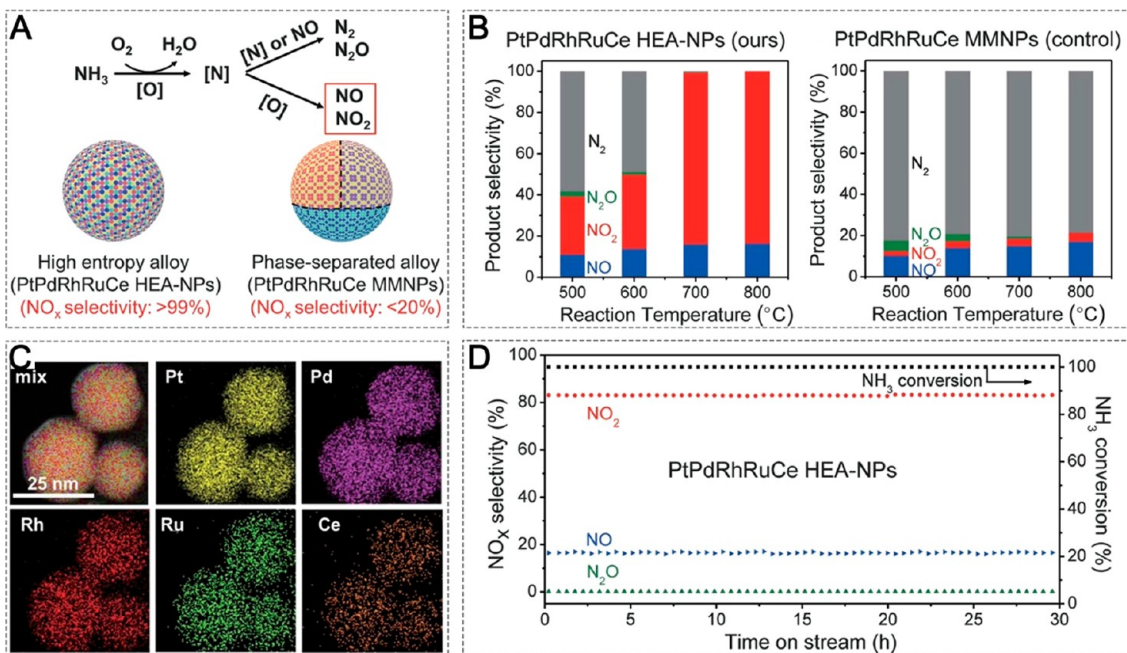


**Figure 9.** (A) Reaction scheme for the ammonia oxidation process and structural and performance differences between the PtPdRhRuCe HEA NPs and phase-separated PtPdRhRuCe. (B) Temperature-dependent product distribution and conversion of  $\text{NH}_3$  for PtPdRhRuCe HEA NPs and phase-separated PtPdRhRuCe. (C) Elemental maps for PtPdRhRuCe HEA NPs. (D) The time-dependent catalytic performance of PtPdRhRuCe HEA NPs at 700 °C. (A–D) Reproduced with permission from ref 29. Copyright 2018 American Association for the Advancement of Science.

(Figure 8A).<sup>27</sup> Quinary CoMoFeNiCu HEA NPs are prepared with facile regulation over the Co/Mo ratio in a wide region. These HEA NPs exhibit substantially enhanced catalytic activity and stability for the decomposition of ammonia. As for mechanistic studies, the binding strength of nitrogen is selected

as the catalytic descriptor to correlate catalytic activity. A typical volcano-type catalytic behavior independent of the Co/Mo ratio is observed for HEA NPs (Figure 8B). According to the Sabatier principle, the catalysts with higher composition of Co element bind to nitrogen species too weak to enhance the kinetic barriers

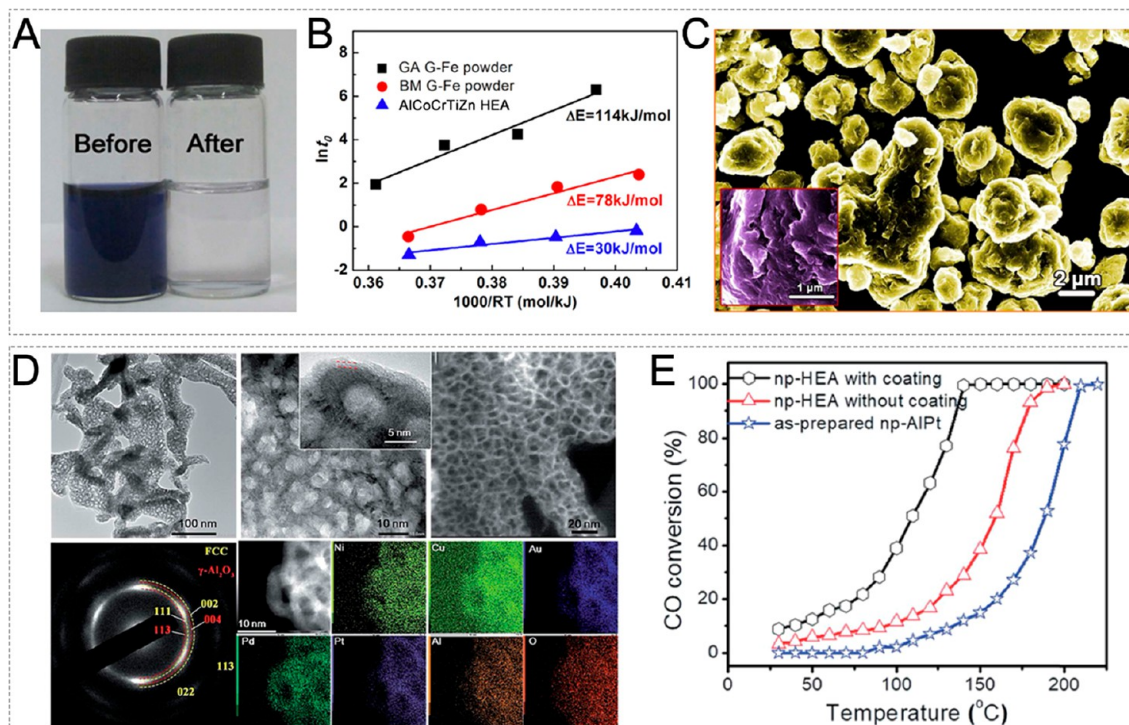


**Figure 10.** (A) Appearances of azo-dyes solution before and after degradation by AlCoCrTiZn HEA. (B) Plot of ( $\ln t_0$ ) vs  $(1000/RT)$  for the estimation of the degradation activation energy for gas-atomization Fe-based glassy (GA G-Fe) powder, ball-milled Fe-based metallic glass (BM G-Fe) powder, and AlCoCrTiZn HEA powder. (C) SEM image of AlCoCrTiZn HEA powders. (A–C) Reproduced with permission from ref 30. Copyright 2016 Springer Nature. (D) TEM images different magnifications, dark-field STEM image, and STEM-EDS mapping of AlNiCuPtPdAu porous HEA. (E) CO conversion as a function of the reaction temperature over AlNiCuPtPdAu porous HEA with and without oxide coating. (D–E) Reproduced with permission from ref 32. Copyright 2019 Royal Society of Chemistry.

for dehydrogenation, while the binding of nitrogen species on the catalysts with higher composition of the Mo element is too strong for the recombination and desorption of  $\text{N}_2$  (Figure 8C).<sup>25</sup> With an optimized Co/Mo ratio, HEA-Co<sub>25</sub>Mo<sub>45</sub> NPs exhibit a mass-specific rate of  $22.1 \text{ gNH}_3 \cdot \text{g}_{\text{metals}}^{-1} \cdot \text{h}^{-1}$  with an improvement factor of  $\sim 19$  versus Co–Mo and have a binding energy of nitrogen value of  $\sim 79 \text{ kJ/mol}$ , very close to that (84 kJ/mol) of Ru nanocrystals (Figure 8C,D).<sup>27</sup> It is worth noting that the optimized Co/Mo ratio in HEA NPs is also influenced by reaction condition, such as the ammonia concentration in the catalytic process. In addition, CoMoFeNiCu HEA NPs also reveal excellent catalytic stability at different temperatures (from 573 to 1000 K), as proved by both experimental tests and Monte Carlo simulations.<sup>27</sup> The robust tunability of the composition as well as the adsorption properties of reactants and intermediates of HEA-based catalysts indicate great potential for the implementation in practical reactors with the catalytic performance optimized under various reaction conditions.

Recently, Wang and co-workers employed another HEA (quinary RuRhCoNiIr) for  $\text{NH}_3$  decomposition.<sup>28</sup> Ru and active non-noble metal Ni exhibit high catalytic activity toward  $\text{NH}_3$  decomposition, but present a large immiscible gap, making the continuous tuning of binary Ru–Ni challenging. Thus, Rh, Co, and Ir are selected to increase the entropy of the system and further contribute to the formation of single-phase alloy.<sup>28</sup> RuRhCoNiIr HEA NPs with an average size of 3–5 nm are facilely fabricated by the CTS method. HAADF-STEM images, XRD profiles, and XANES together confirm the formation of a single-phase alloy (Figure 7).<sup>28</sup> Compared with the RuRhCoNiIr sample with separated phases, RuRhCoNiIr HEA NPs exhibit ca. 5 times higher  $\text{NH}_3$  conversion efficiency at 550 K,

ascribing to the homogeneous alloy structure.<sup>28</sup> Moreover, RuRhCoNiIr HEA NPs show superior stability than previous reported Ru-based catalysts, which benefit from the entropy stabilization effect. The outstanding catalytic performance of RuRhCoNiIr HEA NPs might come from synergistic effect of the ultrafine size, the uniform dispersion, the multielemental composition, and the alloy structure.<sup>28</sup>

**3.2. Ammonia Oxidation Reaction (AOR).** The oxidation of  $\text{NH}_3$  to  $\text{NO}_x$  ( $\text{NO} + \text{NO}_2$ ) is the key processing step in the industrial synthesis. The undesired byproducts of this important reaction are  $\text{N}_2\text{O}$  and  $\text{N}_2$ . Until now, PtPdRh-based multimetallic catalysts are widely employed in industry despite their extremely high cost.<sup>124</sup> Nevertheless, up to 800 °C of reaction temperature is required to promote the yield of  $\text{NO}_x$ , resulting in the degradation of catalysts at such high temperature.<sup>125,126</sup> Besides, the synthesis of solid-solution of PtPdRh multimetallic system is difficult owing to the immiscibility. Yao and his co-worker successfully applied PtPdRhRuCe HEA NPs into AOR to achieve remarkable activity, selectivity, and stability (Figure 9).<sup>29</sup> Pt, Pd, and Rh essentially exhibit excellent catalytic activity toward AOR, and the introduction of Ru and Ce element in HEA NPs not only efficiently reduces the cost of catalysts but also enhances the overall catalytic performance toward  $\text{NH}_3$  via the formation of a highly homogeneous alloy structure. The conversion of  $\text{NH}_3$  reaches 100% with the selectivity for  $\text{NO}_x$  ( $\text{NO} + \text{NO}_2$ ) up to >99% at a relatively low reaction temperature of 700 °C over PtPdRhRuCe HEA NPs (Figure 9D). Compared with PtPdRhRuCe HEA NPs, PtPdRhRuCe multimetallic NPs with separated phases exhibit much lower activity and selectivity for target products (Figure 9B). The enhanced catalytic performance of PtPdRhRuCe HEA NPs is possibly due to the

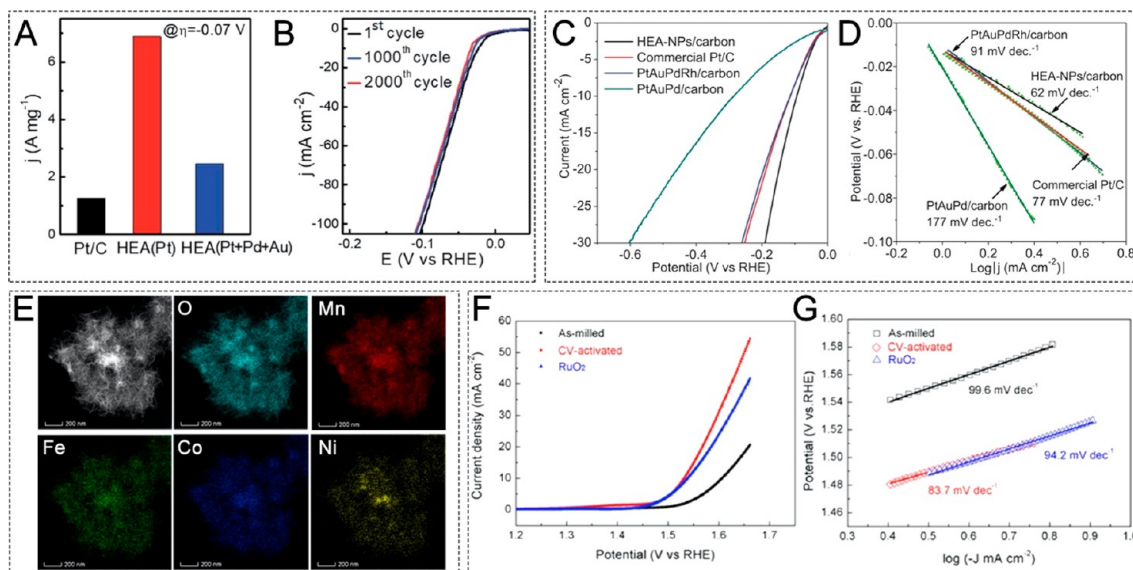


**Figure 11.** (A) Pt and Pt + Pd + Au mass specific activities at 0.07 V and (B) durability test of AlNiCuPtPdAu nanoporous HEA and Pt/C. (A,B) Reproduced with permission from ref 32. Copyright 2019 Royal Society of Chemistry. (C) Polarization curves and (D) Tafel plots of PtAuPdRhRu HEA NPs/carbon, PtAuPdRh/Carbon, PtAuPd/Carbon and commercial Pt/C (Pt loading = 20 wt %) catalysts in 1.0 M KOH. (C,D) Reproduced with permission from ref 35. Copyright 2019 Wiley-VCH. (E) HAADF-STEM image and elemental mappings of the CV-activated MnFeCoNi HEA powders. Electrochemical characterizations of the MnFeCoNi HEA working electrode before and after the CV-activation in 1 M KOH solution (F) linear sweep voltammetry (LSV) curves tested at a scan rate of 5 mV/s and (G) Tafel slopes derived from LSV curves. (E–G) Reproduced with permission from ref 37. Copyright 2019 Elsevier.

highly homogeneous nature to construct distinct highly active sites (Figure 9C). Moreover, no degradation in terms of catalytic activity or selectivity over PtPdRhRuCe HEA NPs is observed in a long-term catalytic test, which is attributed to the high-entropy nature.

**3.3. The Degradation of Azo-Dyes.** Azo-dyes are the largest type of synthetic dyes with azo (-N=N-) functional group or chromophore, which is fairly stable and recalcitrant to degradation.<sup>30</sup> The degradation of azo-dyes is one of the most important reaction in the treatment of environmental pollution and industrial wastewater.<sup>30,116</sup> Currently, zerovalent metals have been extensively exploited in this reaction because of their low cost and high degradation capability.<sup>127–129</sup> Fe- and Mg-based metallic catalysts are the typical zerovalent metals for the degradation of azo-dyes. Unfortunately, the stability of these catalysts is still unsatisfactory. Lv and his co-workers developed highly active and stable zerovalent metals toward the degradation of azo-dyes by applying HEA powders.<sup>30</sup> The blue solution of azo-dyes becomes transparent catalyzed by AlCoCrTiZn, AlCoCrFeNi, and CoCrFeMnNi powders at room temperature for only 10 min (Figure 10A). In addition, the estimated value of apparent energy barrier for AlCoCrTiZn HEA powder is only half that for Fe-based metallic glass (Figure 10B). As for reductive pathway, HEA powders provide electrons for the electron-deficient azo bonds, while hydrogen atoms are derived from water to disassemble the azo dyes into two parts. The excellent catalytic performance of AlCoCrTiZn is ascribed to severe lattice distortion, chemical composition effect, residual stress, and high specific surface area. The lattice distortion makes atoms locate in thermodynamically nonequilibrium positions of the lattice, and HEAs are virtually in a nonequilibrium state. Thus, the atoms in AlCoCrTiZn HEA possess high potential energy, leading to a lower apparent energy barrier. Based on the activity series of metals, the activity sequence of the constituent elements toward azo-dyes degradation is listed as follows: Al >

Ti > Mn > Zn > Cr > Fe > Co > Ni. The higher reactivity of constituents of AlCoCrTiZn HEA results in the faster reaction kinetics than that of AlCoCrFeNi and CoCrFeMnN. In addition, studying the chemical activity of the constituent element is also beneficial to the construction of an efficient catalyst for degradation of azo-dyes. In this work, the ball-milling method causes enhanced specific surface area and a large number of ripples and defects on the surface of HEA powders, contributing to the superior catalytic activity (Figure 10C). Recently, Wu and his co-workers also applied AlFeMnTiM (M = Cr, Co, Ni) HEA powders into the degradation of azo-dyes, where the activity of these HEA powders is superior to that of commercial Fe–Si–B ribbons.<sup>31</sup> The remarkable catalytic activity is proven to be attributed to the unique alloy structure of HEA, the severe lattice distortion, residual stress, and stored plastic deformation energy.

**3.4. CO Oxidation Reaction.** CO oxidation is not only a model reaction to understand the catalytic mechanism at atomic level but also an important industrial reaction in the treatment of automobile exhaust pollution and fuel cells. Au- and Pt-based catalysts are widely used in this reaction in terms of both research and industry, where the high cost of Au and Pt elements and the poisoning of catalysts by CO are the bottlenecks.<sup>130,131</sup> Containing active Au and Pt elements, Qiu et al. applied AlNiCuPtPdAu porous HEA to promote catalytic activity and stability toward CO oxidation.<sup>32</sup> The Al element is selected for the construction of porous structure by dealloying process. Moreover, the residual Al components are naturally oxidized to Al<sub>2</sub>O<sub>3</sub> after cyclic voltammetry activation, forming a layer of oxide thin film on the surface of porous HEA (Figure 10D). Porous HEA coated by oxides exhibits superior catalytic activity relative to porous HEA without coating (Figure 10E). Surface metal–oxygen bonds are regarded to improve the efficiency of dissociating O<sub>2</sub> as the source of atomic oxygen, contributing to the oxidization of CO to CO<sub>2</sub> at a lower kinetic energy barrier.

This step is generally considered as the rate-limiting step for Pt-based catalysts. Moreover, the thin oxides coating possibly prevents the coarsening of AlNiCuPtPdAu porous HEA at high reaction temperature, benefiting the high stability.

**3.5. Electrocatalytic Hydrogen Evolution Reaction (HER).** Hydrogen is one of the most important clean energy sources, and the hydrogen production at low price has attracted tremendous interest around the world.<sup>132,133</sup> HER is a semireaction of electrochemical splitting of water, containing multistep reactions on the surface of catalysts. The reaction steps of HER are different in acidic and alkaline environments, but in both environments, the first step is the Volmer reaction, that is, an electron is transferred to the surface of catalysts followed by interaction with a H<sup>+</sup> to form an adsorbed hydrogen atom (H\*). Volmer reaction is generally considered as the rate-limiting step for HER.<sup>132,133</sup> Typically, Pt- and Pd-based catalysts show excellent catalytic activity in this important reaction. Unfortunately, the high price of noble metals significantly limits sustainable production of hydrogen on a large scale.<sup>34,134</sup> Preparing HEA containing these active metals can lower the cost and meanwhile maintain the catalytic activity. Qiu et al. prepared senary AlNiCuPtPdAu and octonary AlNiCuPtPdAuCoFe nanoporous HEAs with active Pt and Pd components toward HER.<sup>32</sup> The mass activity of Pt element in nanoporous HEAs reaches 6.9 A/mg, 5.5 times as high as that of commercial Pt/C (Figure 11A). As a bonus, nanoporous HEAs also reveal high stability by maintaining initial activity after 2000 cycles (Figure 11B). The outstanding catalytic performance is related to not only the electronic effect, strain effect, and synergistic effect of HEA but also the porous structure with bigger pore size, which facilitates the mass transport and provides an excellent electron transfer network. Besides Pt-based nanoporous HEAs, Ir-based nanoporous HEAs also exhibit comparable electrocatalytic performance when compared to commercial Pt/C.<sup>33</sup> In addition, PtAuPdRhRu HEA NPs were also applied in HER by Dai et al.<sup>35</sup> With the initial overpotential of 25 mV and Tafel slope of 62 mV/dec, the catalytic activity of these HEA NPs is even better than that of commercial Pt/C (Figure 11C,D). The superior electrocatalytic performance of PtAuPdRhRu HEA NPs is ascribed to high-entropy at nanoscale and strong synergistic effects resulting from these different metallic atoms.

Transition metals and their alloys are promising candidates as highly efficient catalysts for HER owing to their partially filled *d* orbitals. Thanks to the efforts from a variety of groups, non-noble metals of Ni, Co, Fe, Cu, and Zn bind H atoms weakly, while Mo, W, Ti, and Nb are able to interact with H atoms strongly.<sup>34,134</sup> Alloying these metallic elements serves as a promising strategy to develop cheap and efficient catalysts for HER because of the synergistic effect, especially for HEA-based catalysts resulting from tunable composition. Kang and his co-workers prepared Ni<sub>20</sub>Fe<sub>20</sub>Mo<sub>10</sub>Co<sub>35</sub>Cr<sub>15</sub> HEA as efficient and stable noble-metal-free electrocatalysts for HER under both acidic and alkaline conditions.<sup>34</sup> Overpotentials of only 107 mV and 172 mV are required for HEA catalysts in acidic and basic solution, respectively. In addition, the initial overpotential and Tafel slope of single-phase HEA are lower than those of dual-phase alloys, even comparable to those of commercial Pt/C. Further mechanism study validates that single-phase HEA has lower charge transfer resistance, contributing to facile charge transfer and electron transport during the HER reactions. Moreover, the undercoordinated surface atoms of single-phase HEA may synergistically promote the interaction of the

electrode with electrolytes, the adsorption of hydrogen, and efficient charge transfer for the HER process.<sup>34</sup>

### 3.6. Electrocatalytic Oxygen Evolution Reaction (OER).

Relative to HER, OER is another half reaction of electrochemical water splitting by producing O<sub>2</sub>. Because it is a complex four-electron/four-proton reaction process, to a large extent, the high kinetic energy overpotential significantly inhibits the rate of water splitting.<sup>135,136</sup> The emphasis of designing the OER catalyst is to improve the efficiency of electron transportation near catalytic centers, as well as the process of adsorption of the active intermediates produced in the OER (such as OOH\* and O\*).<sup>36</sup> Currently, commonly used OER catalysts are IrO<sub>2</sub> and RuO<sub>2</sub>.<sup>38,137</sup> To decrease the price of catalyst, alloying non-noble metals into Ir-based catalysts is a reasonable route. Moreover, the synergistic effect of alloys with unique electronic structures potentially improves the electrocatalytic activity. With active Ir elements, AlNiCoIrMo nanoporous HEA is successfully applied into both OER and HER under acidic condition by Qiu and his co-workers.<sup>32</sup> Thus, AlNiCoIrMo nanoporous HEA can be used as both cathode and anode catalyst at the same time to assemble an electrolytic cell, which delivers better performance than commercially available Pt/C-IrO<sub>2</sub> electrolytic cell. The high catalytic activity of nanoporous HEA is not only due to the porous structures which are conducive to the transportation of gas on the surface but also due to the formed oxides/hydroxides on the surface that adsorb and stabilize a large number of active intermediates during OER process. As for Ir-free catalysts for OER, Waag et al. demonstrated the excellent catalytic performance of equimolar CoCrFeMnNi HEA NPs.<sup>38</sup> At an overpotential of 1.7 V in alkaline solution, the average mass specific activity of these HEA NPs reaches 0.104 A/mg, even comparable to that of commercial IrO<sub>x</sub> catalysts. Pan and his co-workers also proposed a novel OER electrocatalyst based on MnFeCoNi HEA NPs.<sup>37</sup> After an electrochemical cyclic voltammetry (CV) scan activation, MO<sub>x</sub> (M = 1/4Mn, Fe, Co, and Ni) nanosheets grow directly on the surface of MnFeCoNi HEA NPs, forming a core–shell structure (Figure 11E). The MnFeCoNi-based catalyst exhibits a current density of 10 mA/cm<sup>2</sup> at a low overpotential of 302 mV and a small Tafel slope of 83.7 mV/dec, which is comparable to that of RuO<sub>2</sub> (Figure 11F,G).<sup>37</sup> Further investigations manifest the oxidized surface during OER process allows the catalyst to possess a larger surface area and more active sites, thereby improving the catalytic activity of OER. Moreover, the catalyst is highly durable in long-term electrolysis for over 20 h in 1 M KOH alkaline solution, benefiting from the stabilization effect induced by the MO<sub>x</sub> shell.

### 3.7. Electrocatalytic Oxygen Reduction Reaction (ORR).

As the reverse reaction of OER, ORR is also a complex process of four-electron/four-proton, which causes sluggish kinetics.<sup>138,139</sup> More importantly, ORR is a key reaction in the development of fuel cell technology with high performance, attracting considerable attention around the world.<sup>140</sup> Experimentally, Pt-based nanocrystals are the state-of-the-art catalysts for ORR because of their outstanding performance.<sup>141</sup> As for theoretical interpretation and prediction, the binding energies of intermediates (such as O\* and OH\*) are generally the descriptors for catalytic activity because of the well-established Sabatier principle in catalysis.<sup>40,41</sup> For optimized catalysts, the adsorption energy of key intermediates should be neither too strong nor too weak. When it comes to ORR, the activity versus adsorption energy relationship (volcano-type plot) indicates that Pt sites with optimal catalytic performance should bind the

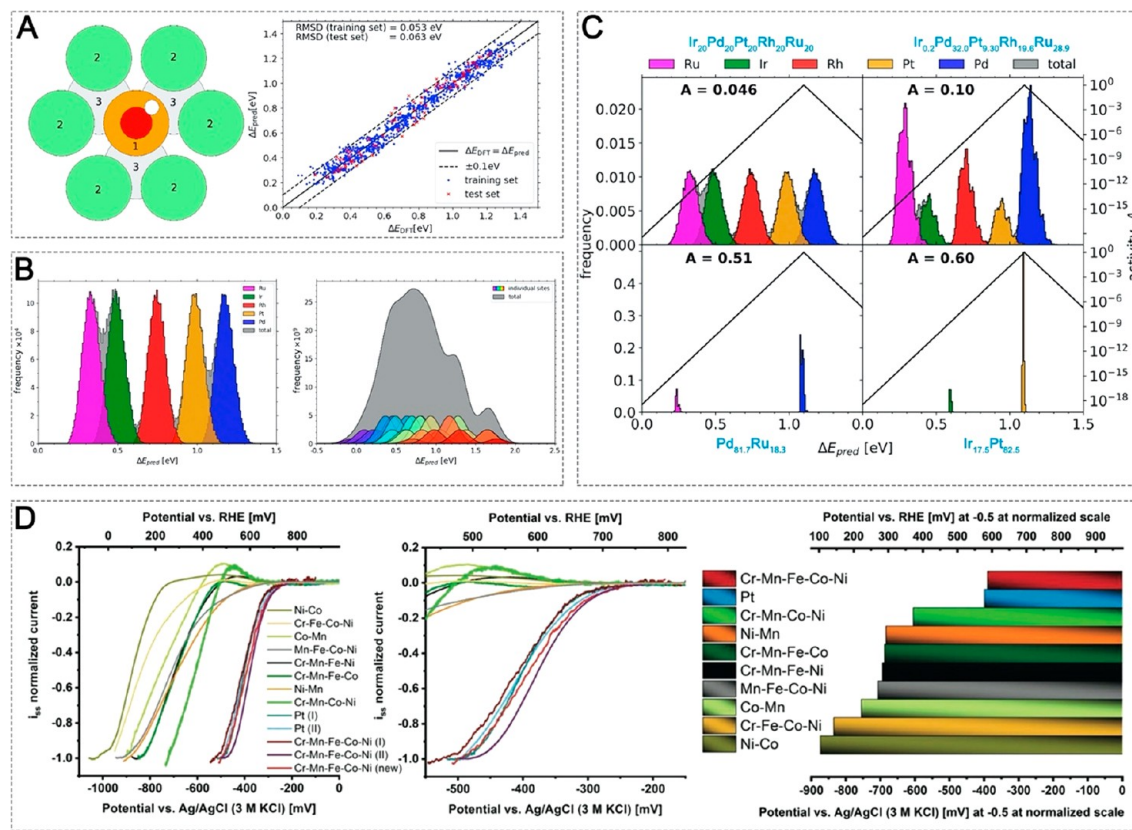


**Figure 12.** (A)  $\text{OH}^*$  adsorbed on HEAs. Each colored zone represents a neighboring shell with a set of five parameters and  $\text{OH}^*$  adsorption model trained on 871 samples (blue dots) and tested on 76 samples (red crosses).<sup>40</sup> (B)  $\text{OH}^*$  and  $\text{O}^*$  adsorption on HEA models.<sup>40</sup> (C) Activities of re-engineered compositions of the  $\text{IrPdPtRhRu}$  HEA.<sup>40</sup> (A–C) Reproduced with permission from ref 40. Copyright 2018 Cell. (D) Comparison of intrinsic activity of different catalysts toward ORR.<sup>39</sup> Reproduced with permission from ref 39. Copyright 2018 Wiley-VCH.

$\text{OH}^* \sim 0.1$  eV lower relative to Pt(111).<sup>41</sup> Recently, Batchelor et al. reported that HEAs provide a near-continuous distribution of adsorption energies and thereby theoretically serve as a design platform for the unbiased discovery of new alloys by promoting sites with exceptional catalytic activity.<sup>40</sup> By calculating the adsorption energy of  $\text{OH}^*$  and  $\text{O}^*$  at the random active sites on the surface of  $\text{IrPdPtRhRu}$  HEA, a database of adsorption energy and a construction function model can be established (a volcanic map) (Figure 12A–C). Thanks to the fact that the composition in HEA is able to be easily adjusted, highly active ORR electrocatalysts could be facilely designed by construction of active sites near the peak of volcanic map on the surface. Optimization of the HEA composition results in the  $\text{Ir}_{10.2}\text{Pd}_{32.0}\text{Pt}_{9.3}\text{Rh}_{19.6}\text{Ru}_{28.9}$  HEAs. Possessing active sites with adsorption energies close to the peak of the volcano curve on the surface,  $\text{Ir}_{10.2}\text{Pd}_{32.0}\text{Pt}_{9.3}\text{Rh}_{19.6}\text{Ru}_{28.9}$  HEAs exhibit lower overpotential even compared with Pt/C. Although the HEAs show enhance catalytic activity for ORR, the cost of catalysts is still high. Excitingly, the Schuhmann group successfully developed non-noble metal catalysts of CrMnFeCoNi HEA NPs for ORR, which even show comparable catalytic performance to commercial Pt/C (Figure 12D).<sup>39</sup> Systematic removal of each metallic element form CrMnFeCoNi HEA NPs to form quaternary alloys all significantly decreases the catalytic activity. The remarkable catalytic performance of HEA NPs is probably based on the typical properties of the constituents. Furthermore, the high-entropy induced single solid solution phase results in a homogeneous distribution of all components, potentially

constructing a larger number of novel active sites for ORR and further improve the catalytic performance.

**3.8. Electrocatalytic Methanol Oxidation Reaction (MOR).** Besides hydrogen energy source, direct methanol fuel cells (DMFCs) have attracted widespread attention in the market because of their high energy conversion efficiency, low pollutant emissions, simple battery structure, and portability.<sup>142,143</sup> MOR at the anode of a methanol fuel cell requires efficient catalysts, which is also mainly catalyzed by noble-metal Pt-based catalysts. Toxic CO will generate as the intermediate during MOR to poison Pt-based catalysts by strongly binding to surface Pt atoms.<sup>144</sup> Tsai and his co-workers reported Pt-based  $\text{Pt}_{50}\text{Fe}_{11}\text{Co}_{10}\text{Ni}_{11}\text{Cu}_{10}\text{Ag}_{8}$  HEA film as a highly active and stable catalyst toward MOR.<sup>42</sup> The enhanced entropy may be responsible for the superior catalytic performance relative to that of Pt. In addition, hcp-structured HEA with high stability was also applied into MOR by Yusenko et al.<sup>43</sup> Pt group metals and rhenium (Re) are reported to be ideal candidates for the construction of HEAs with hcp structure, thus single-phase hcp- $\text{Ir}_{0.19}\text{Os}_{0.22}\text{Re}_{0.21}\text{Rh}_{0.20}\text{Ru}_{0.19}$  HEA is successfully fabricated for MOR, showing superior catalytic properties relative to monometallic counterparts. The electrooxidation of methanol under acidic conditions is usually divided into two steps. The first step is the adsorption and dehydrogenation of methanol molecules on the catalyst surface, and the second step is the oxidation of the adsorbate to  $\text{CO}_2$ . The high electrocatalytic activity of hcp- $\text{Ir}_{0.19}\text{Os}_{0.22}\text{Re}_{0.21}\text{Rh}_{0.20}\text{Ru}_{0.19}$  HEA is probably owing to the electronic effect of alloying or the synergistic effect of HEAs. The unique electronic structure of HEA-based

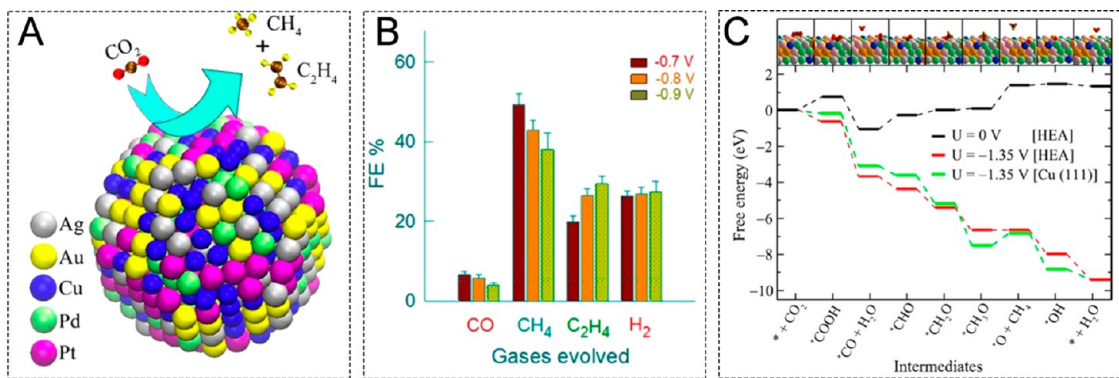


**Figure 13.** (A) Schematic illustration of AuAgPtPdCu HEA NPs catalyzed CO<sub>2</sub>RR. (B) Bar diagram for the FE of their respective carbonaceous species and hydrogen gaseous products at different potentials. (C) Free-energy diagram of CO<sub>2</sub>RR on the surface of AuAgPtPdCu HEA NPs. Optimized structures of all of the intermediates on the HEA surface are shown in the inset. Gray, green, pink, yellow, blue, brown, red, and orange spheres represent Pt, Pd, Ag, Au, Cu, C, O, and H atoms, respectively. (A–C) Reproduced with permission from ref 45. Copyright 2020 American Chemical Society.

catalysts could regulate the valence bond structure of Pt group metal elements to weaken the adsorption ability for CO, contributing to the enhanced catalytic activity toward MOR. The synergistic effect indicates that platinum atoms efficiently adsorb methanol molecule, while transition metal provides surface oxides to oxidize the adsorbed methanol at lower potentials.

**3.9. CO<sub>2</sub> Reduction Reaction (CO<sub>2</sub>RR).** Conversion of CO<sub>2</sub> into valuable chemical fuels not only offers a sustainable method for the production of renewable energy sources, but also alleviates CO<sub>2</sub> pollution, which relies on highly efficient and selective catalysts.<sup>145</sup> Cu is the only monometal capable of reducing CO<sub>2</sub> into C<sub>2+</sub> hydrocarbons significant rates owing to the nearly optimal binding strength to \*CO, achieving a balance of the barriers for activation of CO<sub>2</sub> and hydrogenation of \*CO.<sup>44,145</sup> Meanwhile, it binds hydrogen (H) weakly, efficiently suppressing the formation of competitive H<sub>2</sub>.<sup>44,145</sup> Recently, Biswas and co-workers designed equimolar AuAgPtPdCu HEA NPs for electrochemical CO<sub>2</sub>RR based on DFT calculations of \*CO and H adsorption energies of distinct surface sites (Figure 13A).<sup>44,45</sup> It is worth noting that the electrocatalytic activity is predominantly described by the presence of redox-active Cu metal (Cu<sup>2+</sup>/Cu<sup>0</sup>), and other metals provide a synergistic effect. AuAgPtPdCu HEA NPs exhibit a faradic efficiency (FE) of ~100% for the gaseous products (CO, CH<sub>4</sub>, C<sub>2</sub>H<sub>4</sub>, and H<sub>2</sub>) at a low applied potential with negligible liquid product formation (Figure 13B). The calculated free-energy reaction profiles for CO<sub>2</sub>RR reveals that, compared with Cu(111) surface, AuAgPtPdCu HEA NPs possess decreased theoretical limiting potential, ascribing to the destabilization of the \*OCH<sub>3</sub> intermediate and stabilization of the \*O intermediate on the HEA surface (Figure 13C).<sup>45</sup> Moreover, the exothermic process of the adsorption of CO indicates that CO is difficult to be desorbed from the surface of HEA, responsible for the low FE for CO (Figure 13C). Far from the thermoneutral value for efficient HER catalysts, −0.45 eV of free-energy adsorption of H is consistent with the experimental result that the FE for H<sub>2</sub> was lower than that for CH<sub>4</sub> and C<sub>2</sub>H<sub>4</sub>, contributing to the enhanced selectivity of AuAgPtPdCu HEA NPs.<sup>45</sup>

#### 4. CHALLENGES AND OPPORTUNITIES

The research of HAE-based catalysis is just in its infancy, and there are too many open questions for synthetic methods, catalytic reactions, and mechanistic understandings. With the

increase of the number of components, the catalytic system becomes much more complex than their monometallic and bimetallic counterparts. We consider that the most crucial study in the research of metallic catalysis is the identification of active centers. Accurate identification of active centers directly determines the design, fabrication, modification, and further improvement of metallic catalysts. With the continuous study on single-crystal model catalysts in surface science and density functional calculations over the past several decades, the mechanistic understanding has achieved remarkable progress for monometallic and bimetallic catalysts.<sup>146–152</sup> As for HEAs, there are so many possibilities of the arrangement of surface atoms. It is difficult to elucidate the real active centers by the investigation of one or several models. Probably, the study of HEA-based catalysis may introduce novel strategies, such as statistical method, into mechanistic understanding. Focusing on the active centers, we provide the future development directions in HEA-based catalysis based on the best of the authors' knowledge. These directions are both challenges and opportunities for HEA-based catalysis and also for heterogeneous catalysis (Figures 9 and 10).

**4.1. Development of Novel Synthetic Methods for HEAs.** Although several synthetic methods for HEA-based catalysts have been reported and also discussed in detail in this Review, these synthetic methods still need to be improved from different aspects.<sup>27–33,35,38,39,42,45,102,114–116</sup> Therefore, developing novel synthetic routes for the construction of HEAs with controlled composition, size, and uniformity is still urgently desired. Moreover, HEAs are also expected to be prepared at mild condition with high productivity, which is essential for practical application of HEAs as heterogeneous catalysts in chemical industry production and environmental protection.

**4.2. Preparation of HEAs with Distinct Morphologies.** The catalytic activity and selectivity of metallic catalysis are largely affected by the exposed facets of metallic nanocrystals. Tailoring exposed facets sites of catalysts impacts the binding energy of intermediates, further improving catalytic activity and selectivity toward desired products.<sup>153</sup> A notable example is the Pt-based catalysts toward ORR, where Pt<sub>3</sub>Ni(111) nanocrystals exhibit significantly higher catalytic activity than Pt<sub>3</sub>Ni(100), Pt<sub>3</sub>Ni(110), and monometallic Pt nanocrystals from both theoretical and experimental views.<sup>53</sup> In spite of the exposure of the same (111) facets, metallic icosahedrons and decanedrons with twin structures show superior catalytic activity relative to

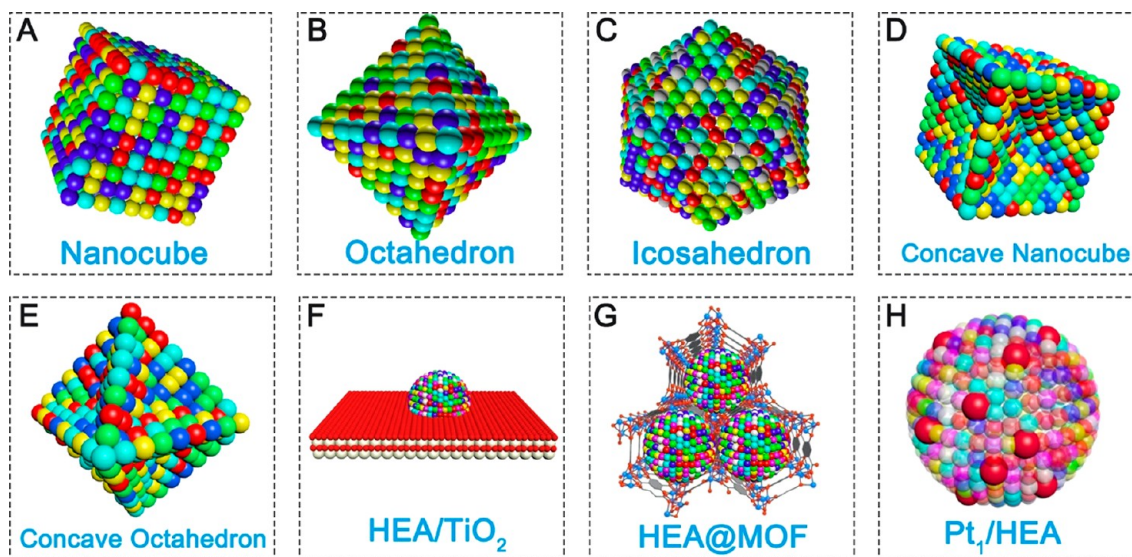


**Figure 14.** (A–E) The models of HEAs with distinct shapes by exposure uniform facets on the surface. (F–H) Schematic illustrations of HEA-based hybrid catalysts.

metallic octahedrons and tetrahedrons.<sup>154,155</sup> In addition, Pt nanocrystals exposed with high-index facets also deliver enhanced catalytic performance because of low coordination numbers of surface metallic atoms.<sup>53,156,157</sup> For monometals and bimetallic alloys, the nanocrystals with a variety of controlled shapes, including octahedrons, nanocubes, concave nanocubes, icosahedrons, ultrathin nanowires, and ultrathin nanosheets, have been successfully prepared in the last two decades, which also greatly contributes to the study of metallic catalysis.<sup>158–166</sup>

Preparation of HEAs with distinct morphologies may pave a novel avenue to the promotion of the catalytic performance of HEAs (Figure 14A–E). Nevertheless, the fine-control of the growth of specific exposed facets remains as a challenge owing to the distinct nucleation/growth kinetics of compositional metals. Fortunately, some progress has been made in morphology control of ternary alloy, where ternary alloy NPs with controlled shape and size are successfully fabricated. The research on preparing HEAs with distinct morphologies is able to gain inspiration from these works.<sup>167,168</sup> Zhang et al. successfully prepared PtMnCu alloys with distinct morphologies with glycine and poly(vinylpyrrolidone) (PVP) serving as the reduction and capping agents.<sup>167</sup> PVP shows superior reduction capability relative to glycine, while glycine mainly functions as the protecting agent due to the intimate coordination of metal precursor ions with the function groups of glycine. The presence of glycine slows down the reduction rate of metal precursor ions. Thus, changing the mass ratio of PVP/glycine affects the nucleation rate of different metal precursors and also the size as well as exposed facets of NPs. By deliberately regulating the amounts of PVP and glycine, PtMnCu alloys with well-defined morphology are successfully obtained. When 370 mg PVP and 30 mg glycine are added in the system, the highly selective cubic PtMnCu NPs are observed. By reducing the amount of PVP from 370 to 220 mg while keeping other synthetic conditions identical, PtMnCu with concave nanocubes (CNC), nano-flower, and ramiform polyhedron (RP) structures are fabricated with uniform size and well-defined morphology. Moreover, PtMnCu NPs with CNC and RP structures are observed to be enclosed by high-index facets, which induces a high density of low-coordination Pt sites and further contributes to the

enhanced catalytic activity for MOR. The Mirkin group applied an alloying/dealloy method to synthesize multimetallic heterostructured NPs with high-index facets.<sup>168</sup> In this strategy, the formation of high-index facets is achieved by alloying and dealoying metal NPs with foreign shape-regulation metals (Bi, Sb, Pb, Te, etc.) during high-temperature thermal treatment. Taking the preparation of PtRuPd alloy as an example, the metal salt precursors of Pt, Ru, and Pd are coated on a silicon wafer, followed by thermal treatment in Ar atmosphere with pure Bi powders at 1000 °C. Bi powders are first transferred to the silicon wafer with metal precursors via evaporation under high temperature. The mixture is further annealed to dealoy Bi elements from the NPs, then PtRuPd alloys enclosed by {210} high-index facets are successfully obtained. Moreover, confining metal precursors inside individual polymer nanoreactors and separating each reactor within arrays could achieve precise composition and size control of the prepared particles. These methods may also be applicable for designing HEAs with controllable morphologies. Rationally adjusting the usage of reducing agents, capping agents, surface stabilizer, and growth modifier or introducing foreign shape-regulation metal into HEAs serves as a feasible strategy to achieve morphology control of HEAs.

#### 4.3. Construction of HEA-Based Hybrid Catalysts.

Constructing hybrid catalysts is a popular approach to boost the catalytic performance in monometallic and bimetallic catalysis, such as core–shell structure, supported metal NPs, metal NPs@metal–organic frameworks (MOFs), and so on.<sup>170–190,200,201</sup> For example, the core–shell structure is able to significantly prevent the oxidation of metal NPs core, thus promoting the long-term stability of catalysts.<sup>200,201</sup> Besides, severe strain is induced by the lattice mismatch between different atomic layers with different compositions, affecting the binding modes of intermediates and further the catalytic selectivity.<sup>58,70</sup>

As for the supported metal NPs, the structures and electronic properties of the support have a significant influence on metal NPs. Interfaces form between metal NPs and substrates when loading metal NPs onto substrates, which possess distinct coordination environments and thus serve as potential active

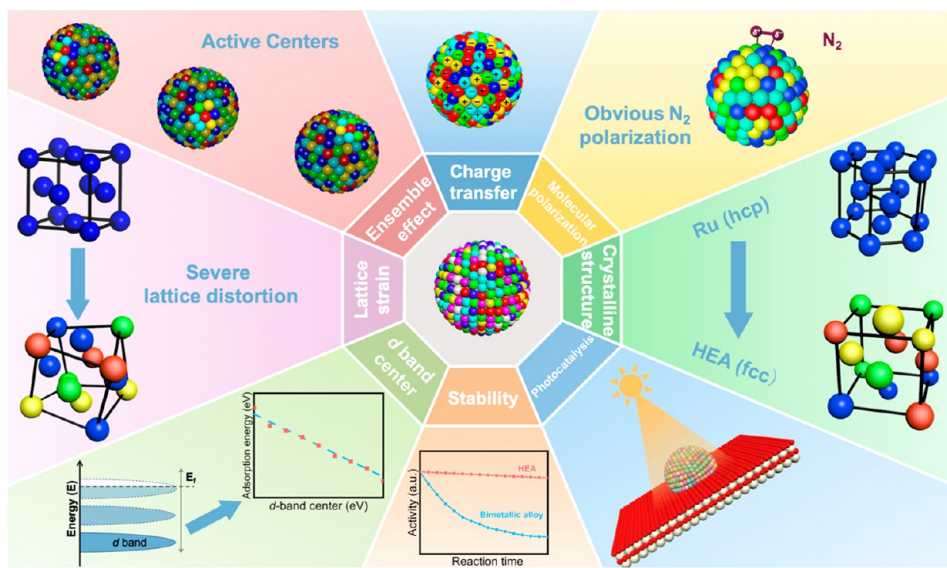


**Figure 15.** Schematic illustration of the proposed future development directions for HEA-based catalysis.

sites for catalytic reactions.<sup>169</sup> Besides, the Mott–Schottky barrier is easily formed at the interface owing to the different work function, which benefits the separation of charge carriers and prolongs the lifetime of hot electrons for the photocatalytic process.<sup>117</sup> Charge transfer also occurs between metal NPs and substrates, which alters the electronic structures of supported metal NPs.<sup>169</sup> Moreover, substrate is able to anchor or bond to metal NPs, preventing metal NPs from segregation or leaching.<sup>28,119</sup>

MOFs represent a class of functional porous materials with high surface areas as well as uniform and fine-tunable pore structures.<sup>170–172</sup> When encapsulated within MOFs’ layers or channels, the catalytic activity of the entire metal NPs surface is able to be promoted, while efficient reactant and product transport are still maintained owing to the porous nature of MOFs.<sup>173</sup> In addition, the electronic structure of metal NPs is altered by the chemical environments of MOFs, affecting the catalytic activity and selectivity.<sup>174</sup> Besides metal NPs, MOFs are capable of serving as active centers as well, and the synergistic effect between metal NPs and MOFs also contributes to one-pot multistep cascade conversion via incorporating the different functions of NPs and MOFs.<sup>175</sup> With uniform and tunable pore size, MOFs are able to serve as a molecular sieve for NPs@MOFs composite materials, which selectively allow reactant molecules with smaller size than the pore size of MOFs to pass through and reach the NPs active sites.<sup>177,178</sup> Thus, finely adjusting the pore size of MOFs is capable of efficiently enhancing the product selectivity owing to this size selectivity effect. MOFs also interact with reactants first in some reactions, lowering the energy barrier for active NPs and further enhancing the catalytic activity and selectivity for specific products.<sup>173</sup> From the perspective of stability, confining metal NPs within the pores of MOFs substrates efficiently prevents the aggregation of NPs, thus enhancing the stability of NPs.<sup>179</sup>

Nowadays, the study of HEA-based catalysts still mainly focuses on the properties of HEAs themselves. Inspired by the results of monometallic and bimetallic catalysis, construction of HEA-based hybrid catalysts serves as a competitive and efficient strategy to design highly active catalysts. HEA-based core–shell structure potentially shows high activity and stability during catalytic reactions. For instance, MnFeCoNi HEA NPs coated

with a thin layer of oxides exhibit excellent stability during long-term electrocatalytic OER, ascribing to the enhanced stability induced by the oxides’ shell.<sup>37</sup> Besides, various interfaces form when HEA NPs interact with distinct substrates, such as HEA–metal interface, HEA–metal oxide interface, HEA–carbon interface, HEA–polymer interface, and so on (Figure 14F). Finely controlling the atomic and electronic structure of the interface is capable of governing the adsorption modes of reactants or intermediates, further providing more active centers or enhancing the selectivity for expected product. In addition, the Mott–Schottky barrier is also able to form at the interface, accelerating the separation of charge carriers during HEAs-catalyzed photoreactions. The electronic structure of HEA NPs, such as *d*-band center, is impacted by the supports. Choosing a suitable substrate to rationally control the position of *d*-band center serves as a novel route to regulate the product selectivity. The interaction between HEA NPs and substrate also promote the catalytic stability of HEA NPs via charge transfer, bonding, and so on. Recently, Hu et al. fabricated RuRhCoNiIr HEA NPs on the carbon support for NH<sub>3</sub> decomposition. The defect on carbon fibers anchors these HEA NPs onto the substrates and further improve the thermal stability.<sup>28</sup> Furthermore, embedding HEAs in MOFs not only potentially restricts the size of HEAs by the pores in MOFs but also regulates the catalytic selectivity via the size control of reactant and product molecules (Figure 14G). Anchoring isolated active atoms on the surface of non-noble metals to form single-atom alloys is an efficient strategy to elevate the usage efficiency of active metals (Figure 14H). The unique coordination environment of single-atom alloys also contributes to the excellent catalytic performance in a number of catalytic reactions, such as selective hydrogenation and oxidation.<sup>182–185</sup>

**4.4. Ensemble Effect for HEAs.** The ensemble effect loosely refers to the influence of geometric arrangements of surface atoms on the catalytic performance after alloying process.<sup>61,62</sup> Composed of multiple metal atoms, different ensembles on the alloy surface exhibit various chemisorption behavior toward reactants or intermediates, providing more suitable active centers for distinct steps during reaction process.<sup>62,63</sup> For HEAs with multiple elements, a specific atom on the surface of HEAs is always surrounded by neighboring

atoms, which also constructs a catalytic ensemble containing central atom and neighboring atoms in metallic catalysis. There are quantities of possible atom arrangements on the surface of HEAs, inducing different adsorption modes of reactants and intermediates. Finely modulating the surface geometry structure of HEAs is able to tuning the adsorption modes for reactant or intermediates, achieving high reaction rates, and selectivity toward desired products. Nevertheless, it is worth noting that the analysis of ensembles in HEAs is extremely complex because of the multiple components and the random distribution of metal atoms. Taking Pt-based HEAs toward ORR as an example, Pt atoms are generally considered as the active atoms rather than the active centers. The active centers are the ensembles of central Pt atoms and their neighboring atoms, where the electronic and geometrical structures of active Pt atoms are determined by these neighboring atoms.<sup>141,191–193</sup> For HEAs, the possibilities of the arrangement of Pt atoms are numerous, and even the coordination environment of each Pt atom is different (Figure 15). When it comes to Pt-free HEAs for ORR, such as CrMnFeCoNi HEA NPs reported by Schuhmann group, even the identification of active atoms becomes a grand challenge.<sup>39</sup> As systematic removal of each metallic element from CrMnFeCoNi HEA NPs to form quaternary alloys significantly decreases the catalytic activity, this may indicate the absence of specific active atoms. The excellent catalytic activity of CrMnFeCoNi HEA NPs for ORR probably results from “cocktail” effect of HEAs. In HEAs, it is unreasonable to identify a specific ensemble as the active centers like bimetallic alloys. The study of ensemble effect (active centers) for HEAs calls for the novel research methods, such as statistical methods, machine learning, and big data.

**4.5. Regulation of Electronic Properties of HEAs.** The electronic structures of catalysts play a vital role in governing the catalytic performance, mainly including *d*-band centers and charge transfer.

*1. d-Band Centers.* In 1995, Norskov and his co-workers first proposed the theory of *d*-band centers for transition metallic catalysis, indicating a scaling relationship between *d*-band centers of metallic catalysts and the adsorption energy of reactants/intermediates.<sup>50</sup> In the past decades, *d*-band theory has been widely utilized to predict and optimize the catalytic performance of materials, including Pt<sub>3</sub>Ni(111) for ORR and MoS<sub>2</sub> for HER.<sup>53,194,195</sup> The position of *d*-band center of alloy is facilely regulated by varying the compositional elements and corresponding concentrations, further affecting the catalytic activity and selectivity. In general, an upshift of the *d*-band center leads to a stronger metal–molecule interaction, whereas a downshift of the *d*-band center results in weaker binding of reactants, which is also known as the ligand effect.<sup>58,60</sup> As for HEAs, the interaction between *d*-bands of compositional metals assists to alter the *d*-band centers of active components, thus regulating the binding energy of key intermediates and further enhancing the activity and selectivity for expected product. For instance, metallic Ir is integrated with metallic Al, Ni, Co, and Mo to form AlNiCoIrMo nanoporous HEAs for highly efficient OER. The projected density of states (PDOS) indicates the variation of the *d*-band center of Ir after alloying, inducing a stronger covalency of Ir–O bond and further contributing to the enhanced oxygen evolution performance.<sup>33</sup> Facilely changing the compositions of components of HEAs is able to continuously tune the *d*-band centers as well as the adsorption energy of key intermediates for optimum catalytic performance

(Figure 15), which is indicated by Batchelor et al. very recently.<sup>40</sup>

*ii. Charge Transfer.* For most of surface atoms of monometallic nanocrystals, the surface charge density is essentially the same because of the same elemental atoms on surface. Negative electrons may slightly accumulate at the edges and corners of monometallic nanocrystals.<sup>181,196</sup> As for alloys, charge transfer between different surface atoms is able to occur owing to the distinct work functions for metallic components, leading to a significant charge redistribution on the surface of alloys.<sup>47</sup> The change of local charge density benefits for the generation of active sites to adsorb and active reactant molecules.<sup>197</sup> Meanwhile, the charge redistribution also has an influence on *d*-band centers, which alter the adsorption modes of reactants and further the catalytic activity and selectivity.<sup>197</sup> With various compositional metals, HEAs potentially possess severe redistribution of surface charges, inducing the alternative accumulation and scarcity of electrons across the whole surface of HEAs (Figure 15).<sup>198,199</sup> Thus, the charge density of each surface metallic atoms differs from the neighboring atoms in HEAs, creating more active center for chemical transformation.<sup>198,199</sup> Besides, the modulated *d*-band center by charge redistribution is also able to promote the catalytic performance by the proper binding energy of reactants. Thus, rationally selecting the components with distinct work functions for the construction of HEAs is able to control the charge density on the surface of HEAs, contributing to the adsorption and activation of reactants and further enhancement of catalytic performance of HEA-based catalysts.

**4.6. Strain Induced by Severe Lattice Distortion of HEAs.** The lattice distortion due to the atomic size mismatch often results in the generation of strain in alloys, which potentially contributes to the enhancement of catalytic performance. The strain effect induces a thermodynamically non-equilibrium state of alloys and leads to a higher potential energy, thus decreasing the energy barrier during catalytic reactions.<sup>30</sup> Besides, lattice strain is also able to lower the formation energy of defects and promote the generation of abundant defects, such as oxygen vacancies. These defects are capable of serving as active centers and further bringing about higher reaction rate during catalytic process.<sup>202</sup> It is also reported that the coupling effect of strain and defects is beneficial for the catalytic reactions.<sup>203</sup> Furthermore, the strain also governs catalytic performance via the regulation of *d*-band centers, which determine the binding strength and activation energy barriers.<sup>70</sup> Generally, a tensile lattice strain elevates the position of *d*-band center, resulting in a stronger interaction between metals and adsorbates, while compressive strain downshifts the *d*-band center, thereby weakening the binding strength of reactants.<sup>71</sup> Rationally regulating the positions of *d*-band center is capable of altering the adsorption modes of reactants or intermediates, further promoting the catalytic activity and selectivity. For example, Pd icosahedrons show much higher Faraday efficiency of CO in CO<sub>2</sub> electrocatalytic reduction relative to Pd octahedrons, because tensile strain from twin structures of icosahedrons elevates *d*-band centers and further promote activation of CO<sub>2</sub> molecules.<sup>204</sup>

Strain engineering of HEAs is an efficient approach to manipulate the catalytic performance of HEA-based catalysts. The intrinsic severe strain endows HEAs with higher potential energy relative to binary or ternary counterparts. Thus, a lower energy barrier occurs in HEA-catalyzed reactions, facilitating the target chemical transformation. For instance, AlCoCrTiZn

HEAs show remarkable catalytic activity toward the degradation of azo-dyes. The strain effect makes AlCoCrTiZn HEAs virtually in a nonequilibrium state, leading to a lower apparent energy barrier and a rapid degradation rate of azo-dyes.<sup>30</sup> Besides varying composition, the selection of metallic components in terms of the size in HEAs is another rational strategy to regulate electronic properties and promote catalytic performance of HEAs via tuning the lattice strain. In addition, the lattice strain also probably modulates the defect chemistry in HEAs and creates more active centers for the adsorption and transformation of reactants, which needs further exploration.

**4.7. Crystalline Structures of HEAs.** The catalytic performance of metallic catalysts is highly associated with their crystalline structures, such as phase structure, phase compositions, and so on. HEAs serve as a promising platform for the phase engineer to improve catalytic performance. HEAs exhibit different phase evolution trend compared with their binary or ternary counterparts. The compositional elements of binary or ternary alloys often present large immiscible gap with the generation of phase-separated materials or intermetallic compound, which constrains the continuous regulation of the composition ratio and further the catalytic performance.<sup>27,28</sup> For HEAs, the larger configuration entropy facilitates the alloying process, and the formation of stable single phase or ideal solid solution structure rather than a fragile intermetallic compound is more favored. Consequently, HEAs are capable of breaking up the immiscible limitation of elements, which is beneficial for the precise control of element concentrations and further the optimization of catalytic properties. Taking CoMoFeNiCu HEA NPs for the NH<sub>3</sub> decomposition reaction, for example, the introduction of Fe, Ni, and Cu break the immiscible gap between active Co and Mo, assisting to finely tune the Co/Mo ratio and further tailor the catalytic performance.<sup>27</sup> Moreover, it has been reported that the solid-solution alloy structure of HEAs is able to efficiently promote the catalytic activity. For instance, compared with the RuRhCoNiIr sample with simple element blending, fcc-structured RuRhCoNiIr HEA NPs exhibit ca. 5 times higher NH<sub>3</sub> conversion efficiency toward NH<sub>3</sub> decomposition reaction, ascribing to the homogeneous alloy structure.<sup>28</sup>

Besides the single-phase stabilization effect induced by the high entropy, HEAs also alter the phase structures of compositional elements, which is potentially helpful to improve overall catalytic activity. The crystalline structures of catalysts are capable of affecting the density of active centers, which is ascribed to the different exposed facets.<sup>205,206</sup> Distinct exposed facets possess diverse energy barriers toward catalytic reactions, thus metallic catalysts with more exposed facets of lower energy barriers show superior catalytic activity.<sup>205,206</sup> For example, the catalytic activity and selectivity of Co nanocrystals with hcp phase are much higher than those of Co nanocrystals with fcc phase toward Fischer–Tropsch reaction (FTR) because of the different efficiency of activation of CO molecules.<sup>205</sup> Besides, fcc-Ru nanocrystals deliver enhanced catalytic activity than hcp-Ru nanocrystals for FTR, because there are a larger number of exposed facets with modest barrier toward FTR available on fcc-Ru while only a few step edges with a lower barrier exist on hcp-Ru.<sup>206</sup> Incorporating metals into single-phase HEAs is able to achieve the phase transformation of these metals, contributing to the superior catalytic activity. For instance, the most stable phase structure for metallic Ru is hcp structure, while Ru-based HEAs displays fcc structure in most cases, which is probably able to promote the catalytic activity toward some important reactions, such as FTR (Figure 15). Designing HEAs with desired

crystalline structures serves as a promising strategy to boost the catalytic performance for targeted reactions.

**4.8. Molecular Polarization on the Surface of HEAs.** In the catalytic transformation of stable molecules, such as CO, CO<sub>2</sub>, O<sub>2</sub>, and N<sub>2</sub>, the activation of these molecules is generally considered as the rate-limiting step.<sup>207–210</sup> The efficient polarization of reactant molecules is able to activate inert reactant molecules, contributing to a higher catalytic activity by decreasing the activation barrier. For example, W<sub>18</sub>O<sub>49</sub> nanowires doped by Mo atoms serve as excellent catalysts for N<sub>2</sub> photofixation by efficiently polarizing N<sub>2</sub> molecules due to the synergy of surface Mo and W atoms.<sup>211</sup> From the aspect of geometric structure, various ensembles on the surface of HEAs serve as potential active centers to achieve efficient adsorption and polarization of reactants. As for electronic structures, the degree of molecular polarization for adsorbed molecules is relatively weak because of the similar electronic properties of surface atoms for monometallic catalysts. In comparison, the electronic properties of surface metallic atoms in HEAs are strikingly varied due to different kinds of components, highly benefiting to the redistribution of charges of adsorbed molecules (Figure 15). The unique surface charge density facilitates the charge transfer from HEAs to adsorbates, inducing the polarization of inert molecules.

**4.9. Enhanced Stability of HEAs.** Besides activity and selectivity, stability is also one of the most important parameters for heterogeneous catalysts, especially for industrial applications. HEAs are expected as highly stable catalysts because of the high entropy effect and sluggish diffusion effect.<sup>2,7,8,13,14,17,18</sup> For commonly utilized noble-metal-based catalysts, such as Pt-, Au-, Ru-based catalysts, they often suffer from poor stability during catalytic reaction, which severely constrains their practical application in industry.<sup>212,213</sup> For example, Pt NPs tend to aggregate during ORR because of Ostwald ripening, leading to the continuous degeneration of catalytic activity in long-term reaction.<sup>212,213</sup> Besides, the compositional metals in Pt-based binary or ternary alloys are easily leached into the reaction solution, which probably destroys the original structure of catalysts.<sup>212,213</sup> Moreover, toxic species sometimes generate during catalytic process and easily poison the catalysts via strongly binding to the active sites, leading to a declining catalytic stability.<sup>43</sup> Applying HEAs into noble-metal-based catalysts is able to solve these problems. The high entropy and sluggish effect of HEAs promote the thermal stability, alleviating the aggregation or leaching problem of catalysts. For instance, HEAs have exhibited amazing stability toward NH<sub>3</sub> oxidation and decomposition reactions even the reaction temperature up to ~1000 K.<sup>27,29</sup> Furthermore, the interaction between constituent metals in HEAs assists to alter the electronic structure of active noble-metals and further regulate the adsorption energy of toxic intermediates, contributing to the improvement of long-term stability of catalysts. The bottleneck of poor stability of Pt-based alloy electrocatalysts will be hopefully solved by the construction of Pt-based HEAs (Figure 15).

Non-noble metals (Cu, Fe, Co, Ni, etc.) exhibit impressive catalytic activity for various reactions, such as CO<sub>2</sub>RR, HER, OER, and so on.<sup>27–45</sup> Nevertheless, these active metals are extremely unstable under reaction conditions owing to the susceptibility to oxidation and corrosion, which significantly decrease the durability of catalysts. Incorporating active non-noble metals within HEAs is able to promote the resistance of oxidation and corrosion and further the catalytic stability

originating from the slowing sluggish and severe lattice distortion in HEAs. For instance, with high corrosion resistance in both acidic and alkaline solutions, Ni<sub>20</sub>Fe<sub>20</sub>Mo<sub>10</sub>Co<sub>35</sub>Cr<sub>15</sub> HEAs display a negligible decrease of catalytic activities after long-term testing toward HER.<sup>34</sup> Recently, we designed porous CrMnFeCoNi HEAs for the hydrogenation of *p*-nitrophenol.<sup>214</sup> The compositional metals are all in metallic states without the formation of metal oxides based on experimental results, verifying the excellent antioxidation of HEAs. The enhanced oxidation resistance probably benefits for the remarkable catalytic stability of porous CrMnFeCoNi HEA.<sup>214</sup>

**4.10. Application of HEAs into Photocatalysis.** Utilizing sustainable solar energy, photocatalysis has attracted tremendous attention in recent years. HEAs serve as competitive candidates for the construction of a photocatalyst with high-performance owing to the various potential active centers on surface induced by their unique geometric and electronic structures. Until now, there are still no reports on the application of HEAs into photocatalysis. The answer for the possibility of application HEAs as photocatalysts is certainly yes. One strategy to realize light-driven reactions is the introduction of plasmonic metals, such as Au, Ag, and Cu with strong localized surface plasmon resonance effect at visible regions, into HEAs. The hot electrons induced by surface plasmon resonance will inject into antibonding orbitals of adsorbed molecules to promote the activation and transformation of reactants.<sup>215–217</sup> Another strategy is directly loading HEAs on the surface of semiconductors like TiO<sub>2</sub> (Figure 15).<sup>218–220</sup> The hot electrons generated by the electron transition from valence band to conduction band will also transfer to loaded HEAs and thereby accelerate the catalytic process over HEAs. Besides these two methods, combining HEAs with photosensitizers also enhances the capability of photon-adsorption. Photosensitizers with charge-separated excited states assist to accomplish photon-to-electron transformation, followed by the delivery of energetic electrons to active HEAs for further chemical transformation.<sup>221</sup> Rational design and precise construction of HEA-based photocatalysts not only efficiently harvest environment friendly sunlight but also further promote the catalytic performance of HEAs.

In conclusion, the recent progress concerning HEA-based catalysis is systematically summarized in this Review in terms of synthetic methods and catalytic reactions. Moreover, the challenges and future opportunities for this research area are carefully discussed. There are so many open questions and promising directions to be explored, including novel synthetic methods, regulation of electronic properties, identification of active centers, and applications into photocatalysis. The study of HEA-based catalysis is attracting ever increasing attention across different subjects. We believe that with the continuous efforts from a number of groups, HEA-based catalysts possess enormous prospects and will be taken into practical application in the near future.

## AUTHOR INFORMATION

### Corresponding Author

Liangbing Wang – State Key Laboratory for Powder Metallurgy, School of Materials Science and Engineering and Key Laboratory of Electronic Packing and Advanced Functional Materials of Hunan Province, Central South University, Changsha, Hunan 410083, P. R. China;  orcid.org/0000-0003-0913-4067;  
Email: wanglb@csu.edu.cn

### Authors

Yue Xin – State Key Laboratory for Powder Metallurgy, School of Materials Science and Engineering, Central South University, Changsha, Hunan 410083, P. R. China

Shuhui Li – State Key Laboratory for Powder Metallurgy, School of Materials Science and Engineering, Central South University, Changsha, Hunan 410083, P. R. China

Yayang Qian – State Key Laboratory for Powder Metallurgy, School of Materials Science and Engineering, Central South University, Changsha, Hunan 410083, P. R. China

Wenkun Zhu – State Key Laboratory of Environment-friendly Energy Materials, Southwest University of Science and Technology, Mianyang, Sichuan 621010, P. R. China;  
 orcid.org/0000-0002-4116-6213

Haibo Yuan – State Key Laboratory for Powder Metallurgy, School of Materials Science and Engineering, Central South University, Changsha, Hunan 410083, P. R. China

Pengyan Jiang – State Key Laboratory for Powder Metallurgy, School of Materials Science and Engineering, Central South University, Changsha, Hunan 410083, P. R. China

Ruihan Guo – State Key Laboratory for Powder Metallurgy, School of Materials Science and Engineering, Central South University, Changsha, Hunan 410083, P. R. China

Complete contact information is available at:

<https://pubs.acs.org/10.1021/acscatal.0c03617>

### Author Contributions

<sup>†</sup>Y.X., S.L., and Y.Q. contributed equally to this work.

### Notes

The authors declare no competing financial interest.

## ACKNOWLEDGMENTS

This work was supported by National Natural Science Foundation of China (Grant Nos. 51801235, 11875258, 11505187, 51374255, 51802356, 51572299 and 41701359), Innovation-Driven Project of Central South University (No. 2018CX004), the Start-up Funding of Central South University (No. 502045005), the Fundamental Research Funds for the Central Universities (Nos. WK2310000066, WK2060190081). Users with Excellence Program of Hefei Science Center CAS (No. 2019HSC-UE004).

## REFERENCES

- (1) Cantor, B.; Chang, I. T. H.; Knight, P.; Vincent, A. J. B. Microstructural Development in Equiatomic Multicomponent Alloys. *Mater. Sci. Eng., A* **2004**, *375–377*, 213–218.
- (2) Yeh, J. W.; Chen, S. K.; Lin, S. J.; Gan, J. Y.; Chin, T. S.; Shun, T. T.; Tsau, C. H.; Chang, S. Y. Nanostructured High-Entropy Alloys with Multiple Principal Elements: Novel Alloy Design Concepts and Outcomes. *Adv. Eng. Mater.* **2004**, *6*, 299–303.
- (3) Peker, A.; Johnson, W. L. A Highly Processable Metallic Glass: Zr<sub>41.2</sub>Ti<sub>13.8</sub>Cu<sub>12.5</sub>Ni<sub>10.0</sub>Be<sub>22.5</sub>. *Appl. Phys. Lett.* **1993**, *63*, 2342–2344.
- (4) Inoue, A. Stabilization of Metallic Supercooled Liquid and Bulk Amorphous Alloys. *Acta Mater.* **2000**, *48*, 279–306.
- (5) Choi-Yim, H.; Johnson, W. L. Bulk Metallic Glass Matrix Composites. *Appl. Phys. Lett.* **1997**, *71*, 3808–3810.
- (6) Wang, W. H.; Dong, C.; Shek, C. H. Bulk Metallic Glasses. *Mater. Sci. Eng., R* **2004**, *44*, 45–89.
- (7) Miracle, D. B.; Senkov, O. N. A Critical Review of High Entropy Alloys and Related Concepts. *Acta Mater.* **2017**, *122*, 448–511.
- (8) George, E. P.; Raabe, D.; Ritchie, R. O. High-Entropy Alloys. *Nat. Rev. Mater.* **2019**, *4*, 515–534.
- (9) Zhang, W.; Liaw, P. K.; Zhang, Y. Science and Technology in High-Entropy Alloys. *Sci. China Mater.* **2018**, *61*, 2–22.

- (10) Miracle, D. B.; Miller, J. D.; Senkov, O. N.; Woodward, C.; Uchic, M. D.; Tiley, J. Exploration and Development of High Entropy Alloys for Structural Applications. *Entropy* **2014**, *16*, 494–525.
- (11) Senkov, O. N.; Wilks, G. B.; Miracle, D. B.; Chuang, C. P.; Liaw, P. K. Refractory high-entropy alloys. *Intermetallics* **2010**, *18*, 1758–1765.
- (12) Senkov, O. N.; Wilks, G. B.; Scott, J. M.; Miracle, D. B. Mechanical Properties of  $\text{Nb}_{25}\text{Mo}_{25}\text{Ta}_{25}\text{W}_{25}$  and  $\text{V}_{20}\text{Nb}_{20}\text{Mo}_{20}\text{Ta}_{20}\text{W}_{20}$  refractory high entropy alloys. *Intermetallics* **2011**, *19*, 698–706.
- (13) Zhang, Y.; Zuo, T. T.; Tang, Z.; Gao, M. C.; Dahmen, K. A.; Liaw, P. K.; Lu, Z. P. Microstructures and Properties of High-Entropy Alloys. *Prog. Mater. Sci.* **2014**, *61*, 1–93.
- (14) Yeh, J.-W. Alloy Design Strategies and Future Trends in High-Entropy Alloys. *JOM* **2013**, *65*, 1759–1771.
- (15) Yeh, J. W. Recent Progress in High-Entropy Alloys. *Ann. Chim. Sci. Mater.* **2006**, *31*, 633–648.
- (16) Tsai, M. H.; Yeh, J. W. High-Entropy Alloys: A Critical Review. *Mater. Res. Lett.* **2014**, *2*, 107–123.
- (17) Wang, R.; Tang, Y.; Li, S.; Ai, Y.; Li, Y.; Xiao, B.; Zhu, L. a.; Liu, X.; Bai, S. Effect of Lattice Distortion on the Diffusion Behavior of High-Entropy Alloys. *J. Alloys Compd.* **2020**, *825*, 154099.
- (18) Tong, C. J.; Chen, M. R.; Chen, S. K.; Yeh, J. W.; Shun, T. T.; Lin, S. J.; Chang, S. Y. Mechanical Performance of the  $\text{Al}_x\text{CoCrCuFeNi}$  High-Entropy Alloy System with Multiprincipal Elements. *Metall. Mater. Trans. A* **2005**, *36A*, 1263–1271.
- (19) Tsai, M.-H.; Yeh, J. W.; Gan, J. Y. Diffusion Barrier Properties of  $\text{AlMoNbSiTaTiVZr}$  High-Entropy Alloy Layer between Copper and Silicon. *Thin Solid Films* **2008**, *516*, 5527–5530.
- (20) Tsai, K. Y.; Tsai, M. H.; Yeh, J. W. Sluggish Diffusion in Co-Cr-Fe-Mn-Ni High-Entropy Alloys. *Acta Mater.* **2013**, *61*, 4887–4897.
- (21) Chang, H. W.; Huang, P. K.; Yeh, J. W.; Davison, A.; Tsau, C. H.; Yang, C. C. Influence of Substrate Bias, Deposition Temperature and Post-Deposition Annealing on the Structure and Properties of Multi-Principal-Component ( $\text{AlCrMoSiTi}$ )<sub>N</sub> Coatings. *Surf. Coat. Technol.* **2008**, *202*, 3360–3366.
- (22) Rogachev, A. S.; Vadchenko, S. G.; Kochetov, N. A.; Rouvimov, S.; Kovalev, D. Y.; Shchukin, A. S.; Moskovskikh, D. O.; Nepapushev, A. A.; Mukasyan, A. S. Structure and Properties of Equiatomic  $\text{CoCrFeNiMn}$  Alloy Fabricated by High-Energy Ball Milling and Spark Plasma Sintering. *J. Alloys Compd.* **2019**, *805*, 1237–1245.
- (23) Zhou, Y. J.; Zhang, Y.; Wang, Y. L.; Chen, G. L. Solid Solution Alloys of  $\text{AlCoCrFeNiTi}_x$  with Excellent Room-Temperature, Mechanical Properties. *Appl. Phys. Lett.* **2007**, *90*, 181904.
- (24) Li, C.; Li, J. C.; Zhao, M.; Jiang, Q. Effect of Alloying Elements on Microstructure and Properties of Multiprincipal Elements High-Entropy Alloys. *J. Alloys Compd.* **2009**, *475*, 752–757.
- (25) Rao, Z.; Dutta, B.; Körmann, F.; Ponge, D.; Li, L.; He, J.; Stephenson, L.; Schäfer, L.; Skokov, K.; Gutfleisch, O.; et al. Unveiling the Mechanism of Abnormal Magnetic Behavior of  $\text{FeNiCoMnCu}$  High-Entropy Alloys through a Joint Experimental-Theoretical Study. *Phys. Rev. Mater.* **2020**, *4*, 014402.
- (26) Zhao, R. F.; Ren, B.; Zhang, G.-P.; Liu, Z.-X.; Cai, B.; Zhang, J. J.  $\text{CoCr}_x\text{CuFeMnNi}$  High-Entropy Alloy Powders with Superior Soft Magnetic Properties. *J. Magn. Magn. Mater.* **2019**, *491*, 165574.
- (27) Xie, P.; Yao, Y.; Huang, Z.; Liu, Z.; Zhang, J.; Li, T.; Wang, G.; Shahbazian-Yassar, R.; Hu, L.; Wang, C. Highly Efficient Decomposition of Ammonia Using High-Entropy Alloy Catalysts. *Nat. Commun.* **2019**, *10*, 4011.
- (28) Yao, Y.; Liu, Z.; Xie, P.; Huang, Z.; Li, T.; Morris, D.; Finfrock, Z.; Zhou, J.; Jiao, M.; Gao, J.; et al. Computationally aided, entropy-driven synthesis of highly efficient and durable multi-elemental alloy catalysts. *Sci. Adv.* **2020**, *6*, eaaz0510.
- (29) Yao, Y.; Huang, Z.; Xie, P.; Lacey, S. D.; Jacob, R. J.; Xie, H.; Chen, F.; Nie, A.; Pu, T.; Rehwoldt, M.; et al. Carbothermal Shock Synthesis of High-Entropy-Alloy NPs. *Science* **2018**, *359*, 1489–1494.
- (30) Lv, Z. Y.; Liu, X. J.; Jia, B.; Wang, H.; Wu, Y.; Lu, Z. P. Development of a Novel High-Entropy Alloy with Eminent Efficiency of Degrading Azo Dye Solutions. *Sci. Rep.* **2016**, *6*, 34213.
- (31) Wu, S. K.; Pan, Y.; Wang, N.; Lu, T.; Dai, W. J. Azo Dye Degradation Behavior of  $\text{AlFeMnTiM}$  ( $\text{M} = \text{Cr}, \text{Co}, \text{Ni}$ ) High-Entropy Alloys. *Int. J. Miner., Metall. Mater.* **2019**, *26*, 124–132.
- (32) Qiu, H. J.; Fang, G.; Wen, Y.; Liu, P.; Xie, G.; Liu, X.; Sun, S. Nanoporous High-Entropy Alloys for Highly Stable and Efficient Catalysts. *J. Mater. Chem. A* **2019**, *7*, 6499–6506.
- (33) Jin, Z.; Lv, J.; Jia, H.; Liu, W.; Li, H.; Chen, Z.; Lin, X.; Xie, G.; Liu, X.; Sun, S.; et al. Nanoporous Al-Ni-Co-Ir-Mo High-Entropy Alloy for Record-High Water Splitting Activity in Acidic Environments. *Small* **2019**, *15*, 1904180.
- (34) Zhang, G.; Ming, K.; Kang, J.; Huang, Q.; Zhang, Z.; Zheng, X.; Bi, X. High Entropy Alloy as a Highly Active and Stable Electrocatalyst for Hydrogen Evolution Reaction. *Electrochim. Acta* **2018**, *279*, 19–23.
- (35) Liu, M.; Zhang, Z.; Okejiri, F.; Yang, S.; Zhou, S.; Dai, S. Entropy-Maximized Synthesis of Multimetallic Nanoparticle Catalysts via a Ultrasonication-Assisted Wet Chemistry Method under Ambient Conditions. *Adv. Mater. Interfaces* **2019**, *6*, 1900015.
- (36) Loeffler, T.; Savan, A.; Garzon-Manjon, A.; Meischein, M.; Scheu, C.; Ludwig, A.; Schuhmann, W. Toward a Paradigm Shift in Electrocatalysis Using Complex Solid Solution NPs. *ACS Energy Lett.* **2019**, *4*, 1206–1214.
- (37) Dai, W.; Lu, T.; Pan, Y. Novel and Promising Electrocatalyst for Oxygen Evolution Reaction based on  $\text{MnFeCoNi}$  High Entropy Alloy. *J. Power Sources* **2019**, *430*, 104–111.
- (38) Waag, F.; Li, Y.; Ziefuss, A. R.; Bertin, E.; Kamp, M.; Duppel, V.; Marzun, G.; Kienle, L.; Barcikowski, S.; Goekce, B. Kinetically-Controlled Laser-Synthesis of Colloidal High-Entropy Alloy NPs. *RSC Adv.* **2019**, *9*, 18547–18558.
- (39) Löffler, T.; Meyer, H.; Savan, A.; Wilde, P.; Garzón Manjón, A.; Chen, Y.-T.; Ventosa, E.; Scheu, C.; Ludwig, A.; Schuhmann, W. Discovery of a Multinary Noble Metal-Free Oxygen Reduction Catalyst. *Adv. Energy Mater.* **2018**, *8*, 1802269.
- (40) Batchelor, T. A. A.; Pedersen, J. K.; Winther, S. H.; Castelli, I. E.; Jacobsen, K. W.; Rossmeisl, J. High-Entropy Alloys as a Discovery Platform for Electrocatalysis. *Joule* **2019**, *3*, 834–845.
- (41) Wang, S.; Xin, H. Predicting Catalytic Activity of High-Entropy Alloys for Electrocatalysis. *Chem.* **2019**, *5*, 502–504.
- (42) Tsai, C. F.; Wu, P. W.; Lin, P.; Chao, C.-G.; Yeh, K. Y. Sputter Deposition of Multi-Element NPs as Electrocatalysts for Methanol Oxidation. *Jpn. J. Appl. Phys.* **2008**, *47*, S755–S761.
- (43) Yusenko, K. V.; Riva, S.; Carvalho, P. A.; Yusenko, M. V.; Arnaboldi, S.; Sukhikh, A. S.; Hanfland, M.; Gromilov, S. A. First Hexagonal Close Packed High-Entropy Alloy with Outstanding Stability under Extreme Conditions and Electrocatalytic Activity for Methanol Oxidation. *Scr. Mater.* **2017**, *138*, 22–27.
- (44) Pedersen, J. K.; Batchelor, T. A. A.; Bagger, A.; Rossmeisl, J. High-Entropy Alloys as Catalysts for the  $\text{CO}_2$  and CO Reduction Reactions. *ACS Catal.* **2020**, *10*, 2169–2176.
- (45) Nellaippan, S.; Katiyar, N. K.; Kumar, R.; Parui, A.; Malviya, K. D.; Pradeep, K. G.; Singh, A. K.; Sharma, S.; Tiwary, C. S.; Biswas, K. High-Entropy Alloys as Catalysts for the  $\text{CO}_2$  and CO Reduction Reactions: Experimental Realization. *ACS Catal.* **2020**, *10*, 3658–3663.
- (46) Rodriguez, J. A. Physical and Chemical Properties of Bimetallic Surfaces. *Surf. Sci. Rep.* **1996**, *24*, 223–287.
- (47) Ding, Z. B.; Wu, F.; Wang, Y. C.; Jiang, H. Theoretical Studies of the Work Functions of Pd-based Bimetallic Surfaces. *J. Chem. Phys.* **2015**, *142*, 214706.
- (48) Yang, C.; Wang, N.; Yang, Y.; Huang, S. Effect of Composition and Distribution on Structural and Surface Electronic Properties of Palladium–Gold Bimetallic NPs: a Density Functional Theory Investigation. *Theor. Chem. Acc.* **2015**, *134*, 121.
- (49) Norskov, J. K. Theory of Chemisorption and Heterogeneous Catalysis. *Physica B+C* **1984**, *127*, 193–202.
- (50) Hammer, B.; Norskov, J. K. Electronic Factors Determining the Reactivity of Metal Surfaces. *Surf. Sci.* **1995**, *343*, 211–220.
- (51) Hammer, B.; Norskov, J. K. Why Gold is the Noblest of all the Metals. *Nature* **1995**, *376*, 238–240.

- (52) Xin, H.; Vojodic, A.; Voss, J.; Norskov, J. K.; Abild-Pedersen, F. Effects of *d*-Band Shape on the Surface Reactivity of Transition-Metal Alloys. *Phys. Rev. B: Condens. Matter Mater. Phys.* **2014**, *89*, 115114.
- (53) Stamenkovic, V. R.; Fowler, B.; Mun, B. S.; Wang, G.; Ross, P. N.; Lucas, C. A.; Markovic, N. M. Improved Oxygen Reduction Activity on Pt<sub>3</sub>Ni(111) via Increased Surface Site Availability. *Science* **2007**, *315*, 493–497.
- (54) Long, R.; Li, Y.; Liu, Y.; Chen, S.; Zheng, X.; Gao, C.; He, C.; Chen, N.; Qi, Z.; Song, L.; et al. Isolation of Cu Atoms in Pd Lattice: Forming Highly Selective Sites for Photocatalytic Conversion of CO<sub>2</sub> to CH<sub>4</sub>. *J. Am. Chem. Soc.* **2017**, *139*, 4486–4492.
- (55) Wang, Z.; Song, Y.; Zou, J.; Li, L.; Yu, Y.; Wu, L. The Cooperation Effect in the Au-Pd/LDH for Promoting Photocatalytic Selective Oxidation of Benzyl Alcohol. *Catal. Sci. Technol.* **2018**, *8*, 268–275.
- (56) Li, Z.; Gao, L.; Ma, W.; Zhong, Q. Higher Gold Atom Efficiency over Au-Pd/TS-1 Alloy Catalysts for the Direct Propylene Epoxidation with H<sub>2</sub> and O<sub>2</sub>. *Appl. Surf. Sci.* **2019**, *497*, 143749.
- (57) Jin, Z.; Wang, L.; Zuidema, E.; Mondal, K.; Zhang, M.; Zhang, J.; Wang, C.; Meng, X.; Yang, H.; Mesters, C.; et al. Hydrophobic Zeolite Modification for *in Situ* Peroxide Formation in Methane Oxidation to Methanol. *Science* **2020**, *367*, 193–197.
- (58) Yang, Y.; Luo, M.; Zhang, W.; Sun, Y.; Chen, X.; Guo, S. Metal Surface and Interface Energy Electrocatalysis: Fundamentals, Performance Engineering, and Opportunities. *Chem.* **2018**, *4*, 2054–2083.
- (59) Li, C.; Liu, T.; He, T.; Ni, B.; Yuan, Q.; Wang, X. Composition-Driven Shape Evolution to Cu-Rich PtCu Octahedral Alloy Nanocrystals as Superior Bifunctional Catalysts for Methanol Oxidation and Oxygen Reduction Reaction. *Nanoscale* **2018**, *10*, 4670–4674.
- (60) Shao, Q.; Wang, P.; Huang, X. Opportunities and Challenges of Interface Engineering in Bimetallic Nanostructure for Enhanced Electrocatalysis. *Adv. Funct. Mater.* **2019**, *29*, 1806419.
- (61) Gao, F.; Goodman, D. W. Pd-Au Bimetallic Catalysts: Understanding Alloy Effects from Planar Models and (Supported) NPs. *Chem. Soc. Rev.* **2012**, *41*, 8009–8020.
- (62) Li, H.; Shin, K.; Henkelman, G. Effects of Ensembles, Ligand, and Strain on Adsorbate Binding to Alloy Surfaces. *J. Chem. Phys.* **2018**, *149*, 174705.
- (63) Wang, Y.; Cao, L.; Libretto, N. J.; Li, X.; Li, C.; Wan, Y.; He, C.; Lee, J.; Gregg, J.; Zong, H.; et al. Ensemble Effect in Bimetallic Electrocatalysts for CO<sub>2</sub> Reduction. *J. Am. Chem. Soc.* **2019**, *141*, 16635–16642.
- (64) Meng, F.; Yang, M.; Li, Z.; Zhang, R. HCOOH Dissociation over the Pd-Decorated Cu Bimetallic Catalyst: The Role of the Pd Ensemble in Determining the Selectivity and Activity. *Appl. Surf. Sci.* **2020**, *511*, 145554.
- (65) Chen, C.; Kang, Y.; Huo, Z.; Zhu, Z.; Huang, W.; Xin, H. L.; Snyder, J. D.; Li, D.; Herron, J. A.; Mavrikakis, M.; et al. Highly Crystalline Multimetallic Nanoframes with Three-Dimensional Electrocatalytic Surfaces. *Science* **2014**, *343*, 1339–1343.
- (66) Jiang, K.; Shao, Q.; Zhao, D.; Bu, L.; Guo, J.; Huang, X. Phase and Composition Tuning of 1D Platinum-Nickel Nanostructures for Highly Efficient Electrocatalysis. *Adv. Funct. Mater.* **2017**, *27*, 1700830.
- (67) Gong, M.; Deng, Z.; Xiao, D.; Han, L.; Zhao, T.; Lu, Y.; Shen, T.; Liu, X.; Lin, R.; Huang, T.; et al. One-Nanometer-Thick Pt<sub>3</sub>Ni Bimetallic Alloy Nanowires Advanced Oxygen Reduction Reaction: Integrating Multiple Advantages into One Catalyst. *ACS Catal.* **2019**, *9*, 4488–4494.
- (68) Deng, Y.-J.; Tripkovic, V.; Rossmeisl, J.; Arenz, M. Oxygen Reduction Reaction on Pt Overlayers Deposited onto a Gold Film: Ligand, Strain, and Ensemble Effect. *ACS Catal.* **2016**, *6*, 671–676.
- (69) Liu, P.; Norskov, J. K. Ligand and ensemble effects in adsorption on alloy surfaces. *Phys. Chem. Chem. Phys.* **2001**, *3*, 3814–3818.
- (70) Luo, M.; Guo, S. Strain-Controlled Electrocatalysis on Multimetallic Nanomaterials. *Nat. Rev. Mater.* **2017**, *2*, 17059.
- (71) Xia, Z.; Guo, S. Strain Engineering of Metal-Based Nanomaterials for Energy Electrocatalysis. *Chem. Soc. Rev.* **2019**, *48*, 3265–3278.
- (72) Xie, C.; Niu, Z.; Kim, D.; Li, M.; Yang, P. Surface and Interface Control in Nanoparticle Catalysis. *Chem. Rev.* **2020**, *120*, 1184–1249.
- (73) Wang, L. B.; Wang, Y. C.; Guo, H. Y.; Huang, J. L.; Zhao, Y. L.; Liu, Q. Y.; Wu, X.; Zeng, J. Au-Pd Alloy Octapods with High Electrocatalytic Activity for the Oxidation of Formic Acid. *Part. Part. Syst. Charact.* **2015**, *32*, 295–300.
- (74) Chen, P. C.; Liu, G.; Zhou, Y.; Brown, K. A.; Chernyak, N.; Hedrick, J. L.; He, S.; Xie, Z.; Lin, Q. Y.; Dravid, V. P.; et al. Tip-Directed Synthesis of Multimetallic NPs. *J. Am. Chem. Soc.* **2015**, *137*, 9167–9173.
- (75) Gilroy, K. D.; Ruditskiy, A.; Peng, H. C.; Qin, D.; Xia, Y. Bimetallic Nanocrystals: Syntheses, Properties, and Applications. *Chem. Rev.* **2016**, *116*, 10414–10472.
- (76) Kwon, S. G.; Krylova, G.; Phillips, P. J.; Klie, R. F.; Chattopadhyay, S.; Shibata, T.; Bunel, E. E.; Liu, Y.; Prakapenka, V. B.; Lee, B.; et al. Heterogeneous Nucleation and Shape Transformation of Multicomponent Metallic Nanostructures. *Nat. Mater.* **2015**, *14*, 215–223.
- (77) Pi, Y.; Shao, Q.; Wang, P.; Guo, J.; Huang, X. General Formation of Monodisperse IrM (M = Ni, Co, Fe) Bimetallic Nanoclusters as Bifunctional Electrocatalysts for Acidic Overall Water Splitting. *Adv. Funct. Mater.* **2017**, *27*, 1700886.
- (78) Yang, Z. Z.; Liu, L.; Wang, A. J.; Yuan, J.; Feng, J. J.; Xu, Q. Q. Simple Wet-Chemical Strategy for Large-Scaled Synthesis of Snowflake-like PdAu Alloy Nanostructures as Effective Electrocatalysts of Ethanol and Ethylene Glycol Oxidation. *Int. J. Hydrogen Energy* **2017**, *42*, 2034–2044.
- (79) Takahashi, M.; Koizumi, H.; Chun, W. J.; Kori, M.; Imaoka, T.; Yamamoto, K. Finely Controlled Multimetallic Nanocluster Catalysts for Solvent-Free Aerobic Oxidation of Hydrocarbons. *Sci. Adv.* **2017**, *3*, e1700101.
- (80) Nguyen, A. T. N.; Shim, J. H. Seedless, One-Step Synthesis of Porous Pt-Pd Nanoflowers for Electroreduction of Oxygen in Acidic Medium. *Appl. Surf. Sci.* **2018**, *458*, 910–916.
- (81) Yu, H.; Tang, W.; Li, K.; Yin, H.; Zhao, S.; Zhou, S. Design of Cu-based Intermetallic Nanocrystals for Enhancing Hydrogenation Selectivity. *Chem. Eng. Sci.* **2019**, *196*, 402–413.
- (82) Cortie, M. B.; McDonagh, A. M. Synthesis and Optical Properties of Hybrid and Alloy Plasmonic NPs. *Chem. Rev.* **2011**, *111*, 3713–3735.
- (83) Newton, M. A.; Belver-Coldeira, C.; Martinez-Arias, A.; Fernandez-Garcia, M. Dynamic *in Situ* Observation of Rapid Size and Shape Change of Supported Pd NPs during CO/NO Cycling. *Nat. Mater.* **2007**, *6*, 528–532.
- (84) Tao, F.; Grass, M. E.; Zhang, Y.; Butcher, D. R.; Renzas, J. R.; Liu, Z.; Chung, J. Y.; Mun, B. S.; Salmeron, M.; Somorjai, G. A. Reaction-Driven Restructuring of Rh-Pd and Pt-Pd Core-Shell NPs. *Science* **2008**, *322*, 932–934.
- (85) Tao, F.; Dag, S.; Wang, L. W.; Liu, Z.; Butcher, D. R.; Bluhm, H.; Salmeron, M.; Somorjai, G. A. Break-Up of Stepped Platinum Catalyst Surfaces by High CO Coverage. *Science* **2010**, *327*, 850–853.
- (86) Lukas, M.; Meded, V.; Vijayaraghavan, A.; Song, L.; Ajayan, P. M.; Fink, K.; Wenzel, W.; Krupke, R. Catalytic Subsurface Etching of Nanoscale Channels in Graphite. *Nat. Commun.* **2013**, *4*, 1379.
- (87) Combe, N.; Jensen, P.; Pimpinelli, A. Changing Shapes in the Nanoworld. *Phys. Rev. Lett.* **2000**, *85*, 110–113.
- (88) Wang, C. C.; Li, Q. J.; Chen, L.; Cheng, Y. H.; Sun, J.; Shan, Z. W.; Li, J.; Ma, E. Ultrafast Shape Change and Joining of Small-Volume Materials Using Nanoscale Electrical Discharge. *Nano Res.* **2015**, *8*, 2143–2151.
- (89) Frey, N. A.; Peng, S.; Cheng, K.; Sun, S. Magnetic NPs: Synthesis, Functionalization, and Applications in Bioimaging and Magnetic Energy Storage. *Chem. Soc. Rev.* **2009**, *38*, 2532–2542.
- (90) Murty, B. S.; Ranganathan, S. Novel Materials Synthesis by Mechanical Alloying/Milling. *Int. Mater. Rev.* **1998**, *43*, 101–141.
- (91) Suryanarayana, C. Mechanical Alloying and Milling. *Prog. Mater. Sci.* **2001**, *46*, 1–184.
- (92) Xu, W.; Chen, H.; Jie, K.; Yang, Z.; Li, T.; Dai, S. Entropy-Driven Mechanochemical Synthesis of Polymetallic Zeolitic Imidazolate Frameworks for CO<sub>2</sub> Fixation. *Angew. Chem., Int. Ed.* **2019**, *58*, 5018–5022.

- (93) Torimoto, T.; Tsuda, T.; Okazaki, K.-i.; Kuwabata, S. New Frontiers in Materials Science Opened by Ionic Liquids. *Adv. Mater.* **2010**, *22*, 1196–1221.
- (94) Lee, Y. H.; Ren, H.; Wu, E.; Fullerton, E. E.; Meng, Y. S.; Minh, N. Q. All-Sputtered, Superior Power Density Thin-Film Solid Oxide Fuel Cells with a Novel Nanofibrous Ceramic Cathode. *Nano Lett.* **2020**, *20*, 2943.
- (95) Rausch, M.; Golizadeh, M.; Kreiml, P.; Cordill, M. J.; Winkler, J.; Mitterer, C. Sputter Deposition of NiW Films from a Rotatable Target. *Appl. Surf. Sci.* **2020**, *511*, 145616.
- (96) Meischein, M.; Fork, M.; Ludwig, A. On the Effects of Diluted and Mixed Ionic Liquids as Liquid Substrates for the Sputter Synthesis of NPs. *Nanomaterials* **2020**, *10*, 525.
- (97) Shih, C. Y.; Wu, C.; Shugaev, M. V.; Zhigilei, L. V. Atomistic Modeling of Nanoparticle Generation in Short Pulse Laser Ablation of Thin Metal Films in Water. *J. Colloid Interface Sci.* **2017**, *489*, 3–17.
- (98) Lin, Z.; Yue, J.; Liang, L.; Tang, B.; Liu, B.; Ren, L.; Li, Y.; Jiang, L. Rapid Synthesis of Metallic and Alloy Micro/NPs by Laser Ablation towards Water. *Appl. Surf. Sci.* **2020**, *504*, 144461.
- (99) Amendola, V.; Meneghetti, M. What Controls the Composition and the Structure of Nanomaterials Generated by Laser Ablation in Liquid Solution? *Phys. Chem. Chem. Phys.* **2013**, *15*, 3027–3046.
- (100) Letzel, A.; Reich, S.; Rolo, T. d. S.; Kanitz, A.; Hoppius, J.; Rack, A.; Olbinado, M. P.; Ostendorf, A.; Goekce, B.; Plech, A.; et al. Time and Mechanism of Nanoparticle Functionalization by Macromolecular Ligands during Pulsed Laser Ablation in Liquids. *Langmuir* **2019**, *35*, 3038–3047.
- (101) Shih, C. Y.; Streubel, R.; Heberle, J.; Letzel, A.; Shugaev, M. V.; Wu, C.; Schmidt, M.; Goekce, B.; Barcikowski, S.; Zhigilei, L. V. Two Mechanisms of Nanoparticle Generation in Picosecond Laser Ablation in Liquids: the Origin of the Bimodal Size Distribution. *Nanoscale* **2018**, *10*, 6900–6910.
- (102) Bondesgaard, M.; Broge, N. L. N.; Mamakhel, A.; Bremholm, M.; Iversen, B. B. General Solvothermal Synthesis Method for Complete Solubility Range Bimetallic and High-Entropy Alloy Nanocatalysts. *Adv. Funct. Mater.* **2019**, *29*, 1905933.
- (103) Demazeau, G. Solvothermal Reactions: an Original Route for the Synthesis of Novel Materials. *J. Mater. Sci.* **2008**, *43*, 2104–2114.
- (104) Kusada, K.; Kobayashi, H.; Yamamoto, T.; Matsumura, S.; Sumi, N.; Sato, K.; Nagaoka, K.; Kubota, Y.; Kitagawa, H. Discovery of Face-Centered-Cubic Ruthenium NPs: Facile Size-Controlled Synthesis Using the Chemical Reduction Method. *J. Am. Chem. Soc.* **2013**, *135*, 5493–5496.
- (105) Mi, J.-L.; Shen, Y.; Becker, J.; Bremholm, M.; Iversen, B. B. Controlling Allotropism in Ruthenium NPs: A Pulsed-Flow Supercritical Synthesis and *in Situ* Synchrotron X-ray Diffraction Study. *J. Phys. Chem. C* **2014**, *118*, 11104–11110.
- (106) Fan, Z.; Zhang, H. Crystal Phase-Controlled Synthesis, Properties and Applications of Noble Metal Nanomaterials. *Chem. Soc. Rev.* **2016**, *45*, 63–82.
- (107) Cheng, H.; Yang, N.; Lu, Q.; Zhang, Z.; Zhang, H. Syntheses and Properties of Metal Nanomaterials with Novel Crystal Phases. *Adv. Mater.* **2018**, *30*, 1707189.
- (108) Lu, D.; Zhang, Y.; Lin, S.; Wang, L.; Wang, C. Synthesis of PtAu Bimetallic NPs on Graphene-Carbon Nanotube Hybrid Nanomaterials for Nonenzymatic Hydrogen Peroxide Sensor. *Talanta* **2013**, *112*, 111–116.
- (109) Mourdikoudis, S.; Liz-Marzan, L. M. Oleylamine in Nanoparticle Synthesis. *Chem. Mater.* **2013**, *25*, 1465–1476.
- (110) Gedanken, A. Using Sonochemistry for the Fabrication of Nanomaterials. *Ultrason. Sonochem.* **2004**, *11*, 47–55.
- (111) Moghtada, A.; Ashiri, R. Superiority of Sonochemical Processing Method for the Synthesis of Barium Titanate Nanocrystals in Contrast to the Mechanochemical Approach. *Ultrason. Sonochem.* **2018**, *41*, 127–133.
- (112) Wittstock, A.; Zielasek, V.; Biener, J.; Friend, C. M.; Baeumer, M. Nanoporous Gold Catalysts for Selective Gas-Phase Oxidative Coupling of Methanol at Low Temperature. *Science* **2010**, *327*, 319–322.
- (113) Song, R.; Zhang, L.; Zhu, F.; Li, W.; Fu, Z.; Chen, B.; Chen, M.; Zeng, H.; Pan, D. Hierarchical Nanoporous Copper Fabricated by One-Step Dealloying Toward Ultrasensitive Surface-Enhanced Raman Sensing. *Adv. Mater. Interfaces* **2018**, *5*, 1800332.
- (114) Joo, S. H.; Bae, J. W.; Park, W. Y.; Shimada, Y.; Wada, T.; Kim, H. S.; Takeuchi, A.; Konno, T. J.; Kato, H.; Okulov, I. V. Beating Thermal Coarsening in Nanoporous Materials via High-Entropy Design. *Adv. Mater.* **2020**, *32*, 1906160.
- (115) Gao, S.; Hao, S.; Huang, Z.; Yuan, Y.; Han, S.; Lei, L.; Zhang, X.; Shahbazian-Yassar, R.; Lu, J. Synthesis of High-Entropy Alloy Nanoparticles on Supports by the Fast Moving Bed Pyrolysis. *Nat. Commun.* **2020**, *11*, 2016.
- (116) Kumar, N.; Tiwary, C. S.; Biswas, K. Preparation of Nanocrystalline High-Entropy Alloys via Cryomilling of Cast Ingots. *J. Mater. Sci.* **2018**, *53*, 13411–13423.
- (117) Xu, X.; Luo, F.; Tang, W.; Hu, J.; Zeng, H.; Zhou, Y. Enriching Hot Electrons via NIR-Photon-Excited Plasmon in WS<sub>2</sub>@Cu Hybrids for Full-Spectrum Solar Hydrogen Evolution. *Adv. Funct. Mater.* **2018**, *28*, 1804055.
- (118) Wang, H.; Gu, X.-K.; Zheng, X.; Pan, H.; Zhu, J.; Chen, S.; Cao, L.; Li, W.-X.; Lu, J. Disentangling the Size-dependent Geometric and Electronic Effects of Palladium Nanocatalysts beyond Selectivity. *Sci. Adv.* **2019**, *5*, eaat6413.
- (119) Huang, Y.; Liu, Z.; Gao, G.; Xiao, G.; Du, A.; Bottle, S.; Sarina, S.; Zhu, H. Stable Copper Nanoparticle Photocatalysts for Selective Epoxidation of Alkenes with Visible Light. *ACS Catal.* **2017**, *7*, 4975–4985.
- (120) Zhang, L.; Ran, J.; Qiao, S. Z.; Jaroniec, M. Characterization of Semiconductor Photocatalysts. *Chem. Soc. Rev.* **2019**, *48*, 5184–5206.
- (121) Wang, S.; Ichihara, F.; Pang, H.; Chen, H.; Ye, J. Nitrogen Fixation Reaction Derived from Nanostructured Catalytic Materials. *Adv. Funct. Mater.* **2018**, *28*, 1803309.
- (122) Yin, S. F.; Zhang, Q. H.; Xu, B. Q.; Zhu, W. X.; Ng, C. F.; Au, C. T. Investigation on the Catalysis of CO<sub>x</sub>-Free Hydrogen Generation from Ammonia. *J. Catal.* **2004**, *224*, 384–396.
- (123) Jacobsen, C. J. H.; Dahl, S.; Clausen, B. S.; Bahn, S.; Logadottir, A.; Norskov, J. K. Catalyst Design by Interpolation in the Periodic Table: Bimetallic Ammonia Synthesis Catalysts. *J. Am. Chem. Soc.* **2001**, *123*, 8404–8405.
- (124) Wang, C. P.; Wang, J.; Guo, S. H.; Liu, X. J.; Ohnuma, I.; Kainuma, R.; Ishida, K. Experimental Investigation and Thermodynamic Calculation of the Phase Equilibria in the Co–Mo–W System. *Intermetallics* **2009**, *17*, 642–650.
- (125) Hung, C. M. Complex PtPdRh NPs: Synthesis, Characterization, and Performance in the Electrocatalytic Oxidation of Ammonia. *Powder Technol.* **2012**, *232*, 18–23.
- (126) Bagot, P. A. J.; Kruska, K.; Haley, D.; Carrier, X.; Marceau, E.; Moody, M. P.; Smith, G. D. W. Oxidation and Surface Segregation Behavior of a Pt-Pd-Rh Alloy Catalyst. *J. Phys. Chem. C* **2014**, *118*, 26130–26138.
- (127) Chen, X.; Wu, Z.; Liu, D.; Gao, Z. Preparation of ZnO Photocatalyst for the Efficient and Rapid Photocatalytic Degradation of Azo Dyes. *Nanoscale Res. Lett.* **2017**, *12*, 143.
- (128) Shu, H.-Y.; Chang, M.-C.; Yu, H.-H.; Chen, W.-H. Reduction of an Azo Dye Acid Black 24 Solution Using Synthesized Nanoscale Zerovalent Iron Particles. *J. Colloid Interface Sci.* **2007**, *314*, 89–97.
- (129) Mikhailov, I.; Levina, V.; Leybo, D.; Masov, V.; Tagirov, M.; Kuznetsov, D. Synthesis, Characterization and Reactivity of Nanostructured Zero-Valent Iron Particles for Degradation of Azo Dyes. *Int. J. Nanosci.* **2017**, *16*, 1750017.
- (130) Yu, W.; Porosoff, M. D.; Chen, J. G. Review of Pt-based Bimetallic Catalysis: from Model Surfaces to Supported Catalysts. *Chem. Rev.* **2012**, *112*, 5780–5817.
- (131) Zhang, J.; Li, H.; Ye, J.; Cao, Z.; Chen, J.; Kuang, Q.; Zheng, J.; Xie, Z. Sierpinski Gasket-like Pt-Ag Octahedral Alloy Nanocrystals with Enhanced Electrocatalytic Activity and Stability. *Nano Energy* **2019**, *61*, 397–403.
- (132) Song, Q.; Xue, Z.; Liu, C.; Qiao, X.; Liu, L.; Huang, C.; Liu, K.; Li, X.; Lu, Z.; Wang, T. General Strategy to Optimize Gas Evolution

- Reaction via Assembled Striped-Pattern Superlattices. *J. Am. Chem. Soc.* **2020**, *142*, 1857–1863.
- (133) Li, Y.; Wang, H.; Xie, L.; Liang, Y.; Hong, G.; Dai, H. MoS<sub>2</sub> NPs Grown on Graphene: an Advanced Catalyst for the Hydrogen Evolution Reaction. *J. Am. Chem. Soc.* **2011**, *133*, 7296–9.
- (134) Zhang, J.; Wang, T.; Liu, P.; Liao, Z.; Liu, S.; Zhuang, X.; Chen, M.; Zschech, E.; Feng, X. Efficient Hydrogen Production on MoNi<sub>4</sub> Electrocatalysts with Fast Water Dissociation Kinetics. *Nat. Commun.* **2017**, *8*, 15437.
- (135) McKone, J. R.; Sadtler, B. F.; Werlang, C. A.; Lewis, N. S.; Gray, H. B. Ni–Mo Nanopowders for Efficient Electrochemical Hydrogen Evolution. *ACS Catal.* **2013**, *3*, 166–169.
- (136) Trotochaud, L.; Boettcher, S. W. Precise Oxygen Evolution Catalysts: Status and Opportunities. *Scr. Mater.* **2014**, *74*, 25–32.
- (137) Zhang, Y.; Li, Y.; Ni, D.; Chen, Z.; Wang, X.; Bu, Y.; Ao, J.-P. Improvement of BiVO<sub>4</sub> Photoanode Performance During Water Photo-Oxidation Using Rh-Doped SrTiO<sub>3</sub> Perovskite as a Co-Catalyst. *Adv. Funct. Mater.* **2019**, *29*, 1902101.
- (138) Liu, J.; Zheng, Y.; Jiao, Y.; Wang, Z.; Lu, Z.; Vasileff, A.; Qiao, S. Z. NiO as a Bifunctional Promoter for RuO<sub>2</sub> toward Superior Overall Water Splitting. *Small* **2018**, *14*, 1704073.
- (139) Gamler, J. T. L.; Shin, K.; Ashberry, H. M.; Chen, Y.; Bueno, S. L. A.; Tang, Y.; Henkelman, G.; Skrabalak, S. E. Intermetallic Pd<sub>3</sub>Pb Nanocubes with High Selectivity for the 4-Electron Oxygen Reduction Reaction Pathway. *Nanoscale* **2020**, *12*, 2532–2541.
- (140) Kim, H. W.; Lukas, V. J.; Park, H.; Park, S.; Diederichsen, K. M.; Lim, J.; Cho, Y. H.; Kim, J.; Kim, W.; Han, T. H.; Voss, J.; Luntz, A. C.; McCloskey, B. D. Mechanisms of Two-Electron and Four-Electron Electrochemical Oxygen Reduction Reactions at Nitrogen-Doped Reduced Graphene Oxide. *ACS Catal.* **2020**, *10*, 852–863.
- (141) Liang, Y.; Li, Y.; Wang, H.; Zhou, J.; Wang, J.; Regier, T.; Dai, H. Co<sub>3</sub>O<sub>4</sub> Nanocrystals on Graphene as a Synergistic Catalyst for Oxygen Reduction Reaction. *Nat. Mater.* **2011**, *10*, 780–786.
- (142) Shao, M.; Chang, Q.; Dodelet, J.-P.; Chenitz, R. Recent Advances in Electrocatalysts for Oxygen Reduction Reaction. *Chem. Rev.* **2016**, *116*, 3594–3657.
- (143) Tong, Y.; Yan, X.; Liang, J.; Dou, S. X. Metal-Based Electrocatalysts for Methanol Electro-Oxidation: Progress, Opportunities, and Challenges. *Small* **2019**, *19*, 1904126.
- (144) Huang, J.; Liu, Y.; Xu, M.; Wan, C.; Liu, H.; Li, M.; Huang, Z.; Duan, X.; Pan, X.; Huang, Y. PtCuNi Tetrahedra Catalysts with Tailored Surfaces for Efficient Alcohol Oxidation. *Nano Lett.* **2019**, *19*, 5431–5436.
- (145) Nitopi, S.; Bertheussen, E.; Scott, S. B.; Liu, X.; Engstfeld, A. K.; Horch, S.; Seger, B.; Stephens, I. E. L.; Chan, K.; Hahn, C.; Nørskov, J. K.; Jaramillo, T. F.; Chorkendorff, I.; et al. Progress and Perspectives of Electrochemical CO<sub>2</sub> Reduction on Copper in Aqueous Electrolyte. *Chem. Rev.* **2019**, *119*, 7610–7672.
- (146) Choi, J.; Fu, G. C. Transition Metal-Catalyzed Alkyl-Alkyl Bond Formation: Another Dimension in Cross-Coupling Chemistry. *Science* **2017**, *356*, eaaf7230.
- (147) Fu, N.; Sauer, G. S.; Saha, A.; Loo, A.; Lin, S. Metal-Catalyzed Electrochemical Diazidation of Alkenes. *Science* **2017**, *357*, 575–579.
- (148) Seh, Z. W.; Kibsgaard, J.; Dickens, C. F.; Chorkendorff, I. B.; Nørskov, J. K.; Jaramillo, T. F. Combining Theory and Experiment in Electrocatalysis: Insights into Materials Design. *Science* **2017**, *355*, eaad4998.
- (149) Zhou, L.; Swearer, D. F.; Zhang, C.; Robatjazi, H.; Zhao, H.; Henderson, L.; Dong, L.; Christopher, P.; Carter, E. A.; Nordlander, P.; Halas, N. J. Quantifying Hot Carrier and Thermal Contributions in Plasmonic Photocatalysis. *Science* **2018**, *362*, 69–72.
- (150) Luo, M.; Zhao, Z.; Zhang, Y.; Sun, Y.; Xing, Y.; Lv, F.; Yang, Y.; Zhang, X.; Hwang, S.; Qin, Y.; et al. PdMo Bimetallene for Oxygen Reduction Catalysis. *Nature* **2019**, *574*, 81–85.
- (151) Wang, T.; Ibañez, J.; Wang, K.; Fang, L.; Sabbe, M.; Michel, C.; Paul, S.; Pera-Titus, M.; Sautet, P. Rational Design of Selective Metal Catalysts for Alcohol Amination with Ammonia. *Nat. Catal.* **2019**, *2*, 773–779.
- (152) Rao, H.; Schmidt, L. C. S.; Bonin, J.; Robert, M. Visible-Light-Driven Methane Formation from CO<sub>2</sub> with a Molecular Iron Catalyst. *Nature* **2017**, *548*, 74–77.
- (153) Wang, Y.; Wang, Z.; Dinh, C.-T.; Li, J.; Ozden, A.; Golam Kibria, M.; Seifitokaldani, A.; Tan, C.-S.; Gabardo, C. M.; Luo, M.; Zhou, H.; Li, F.; Lum, Y.; McCallum, C.; Xu, Y.; Liu, M.; Proppe, A.; Johnston, A.; Todorovic, P.; Zhuang, T.-T.; Sinton, D.; Kelley, S. O.; Sargent, E. H.; et al. Catalyst Synthesis under CO<sub>2</sub> Electroreduction Favours Faceting and Promotes Renewable Fuels Electrosynthesis. *Nature Catalysis* **2020**, *3*, 98–106.
- (154) Wang, L.; Zhao, S.; Liu, C.; Li, C.; Li, X.; Li, H.; Wang, Y.; Ma, C.; Li, Z.; Zeng, J. Aerobic Oxidation of Cyclohexane on Catalysts Based on Twinned and Single-Crystal Au<sub>75</sub>Pd<sub>25</sub> Bimetallic Nanocrystals. *Nano Lett.* **2015**, *15*, 2875–80.
- (155) Zhou, S.; Zhao, M.; Yang, T. H.; Xia, Y. Decahedral Nanocrystals of Noble Metals: Synthesis, Characterization, and Applications. *Mater. Today* **2019**, *22*, 108–131.
- (156) Bu, L.; Guo, S.; Zhang, X.; Shen, X.; Su, D.; Lu, G.; Zhu, X.; Yao, J.; Guo, J.; Huang, X. Surface Engineering of Hierarchical Platinum–Cobalt Nanowires for Efficient Electrocatalysis. *Nat. Commun.* **2016**, *7*, 11850.
- (157) Huang, L.; Liu, M.; Lin, H.; Xu, Y.; Wu, J.; Dravid, V. P.; Wolverton, C.; Mirkin, C. A. Shape Regulation of High-Index Facet NPs by Dealloying. *Science* **2019**, *365*, 1159–1163.
- (158) Zhang, H.; Jin, M.; Xiong, Y.; Lim, B.; Xia, Y. Shape-Controlled Synthesis of Pd Nanocrystals and Their Catalytic Applications. *Acc. Chem. Res.* **2013**, *46*, 1783–1794.
- (159) Gan, L.; Cui, C.; Heggen, M.; Dionigi, F.; Rudi, S.; Strasser, P. Element-Specific Anisotropic Growth of Shaped Platinum Alloy Nanocrystals. *Science* **2014**, *346*, 1502–1506.
- (160) Zhang, L.; Xie, Z.; Gong, J. Shape-Controlled Synthesis of Au–Pd Bimetallic Nanocrystals for Catalytic Applications. *Chem. Soc. Rev.* **2016**, *45*, 3916–3934.
- (161) Liz-Marzan, L. M.; Grzelczak, M. Growing Anisotropic Crystals at the Nanoscale. *Science* **2017**, *356*, 1120–1121.
- (162) Chen, Z.; Balankura, T.; Fichthorn, K. A.; Rioux, R. M. Revisiting the Polyol Synthesis of Silver Nanostructures: Role of Chloride in Nanocube Formation. *ACS Nano* **2019**, *13*, 1849–1860.
- (163) Wang, S. T.; Lin, Y.; Nielsen, M. H.; Song, C. Y.; Thomas, M. R.; Spicer, C.; Kroger, R.; Ercius, P. A.; Aloni, S.; Stevens, M. M. Shape-controlled Synthesis and *In Situ* Characterisation of Anisotropic Au Nanomaterials Using Liquid Cell Transmission Electron Microscopy. *Nanoscale* **2019**, *11*, 16801–16809.
- (164) Zhao, M.; Chen, Z.; Lyu, Z.; Hood, Z. D.; Xie, M.; Vara, M.; Chi, M.; Xia, Y. Ru Octahedral Nanocrystals with a Face-Centred Cubic Structure, {111} Facets, Thermal Stability up to 400 °C, and Enhanced Catalytic Activity. *J. Am. Chem. Soc.* **2019**, *141*, 7028–7036.
- (165) Yang, T. H.; Shi, Y.; Janssen, A.; Xia, Y. Surface Capping Agents and Their Roles in Shape-Controlled Synthesis of Colloidal Metal Nanocrystals. *Angew. Chem., Int. Ed.* **2020**, *59*, 15378.
- (166) Sun, Y. G.; Xia, Y. N. Shape-Controlled Synthesis of Gold and Silver NPs. *Science* **2002**, *298*, 2176–2179.
- (167) Luan, C.; Zhou, Q.-X.; Wang, Y.; Xiao, Y.; Dai, X.; Huang, X.-L.; Zhang, X. A General Strategy Assisted with Dual Reductants and Dual Protecting Agents for Preparing Pt-Based Alloys with High-Index Facets and Excellent Electrocatalytic Performance. *Small* **2017**, *13*, 1702617.
- (168) Huang, L.; Lin, H.; Zheng, C. Y.; Kluender, E. J.; Golnabi, R.; Shen, B.; Mirkin, C. A. Multimetallic High-Index Faceted Heterostructured Nanoparticles. *J. Am. Chem. Soc.* **2020**, *142*, 4570–4575.
- (169) Liu, L.; Corma, A. Metal Catalysts for Heterogeneous Catalysis: From Single Atoms to Nanoclusters and Nanoparticles. *Chem. Rev.* **2018**, *118*, 4981–5079.
- (170) Hu, M.; Zhao, S.; Liu, S.; Chen, C.; Chen, W.; Zhu, W.; Liang, C.; Cheong, W. C.; Wang, Y.; Yu, Y.; et al. MOF-Confined Sub-2 nm Atomically Ordered Intermetallic PdZn NPs as High-Performance Catalysts for Selective Hydrogenation of Acetylene. *Adv. Mater.* **2018**, *30*, 1801878.

- (171) Li, R.; Zhang, W.; Zhou, K. Metal-Organic-Framework-based Catalysts for Photoreduction of CO<sub>2</sub>. *Adv. Mater.* **2018**, *30*, 1705512.
- (172) Xiao, J. D.; Han, L.; Luo, J.; Yu, S. H.; Jiang, H. L. Integration of Plasmonic Effects and Schottky Junctions into Metal-Organic Framework Composites: Steering Charge Flow for Enhanced Visible-Light Photocatalysis. *Angew. Chem., Int. Ed.* **2018**, *57*, 1103–1107.
- (173) Zhao, M.; Yuan, K.; Wang, Y.; Li, G.; Guo, J.; Gu, L.; Hu, W.; Zhao, H.; Tang, Z. Metal-Organic Frameworks as Selectivity Regulators for Hydrogenation Reactions. *Nature* **2016**, *539*, 76–80.
- (174) Li, X.; Goh, T. W.; Li, L.; Xiao, C.; Guo, Z.; Zeng, X. C.; Huang, W. Controlling Catalytic Properties of Pd Nanoclusters through Their Chemical Environment at the Atomic Level Using Isoreticular Metal–Organic Frameworks. *ACS Catal.* **2016**, *6*, 3461–3468.
- (175) Chen, Y.-Z.; Zhou, Y.-X.; Wang, H.; Lu, J.; Uchida, T.; Xu, Q.; Yu, S.-H.; Jiang, H.-L. Multifunctional PdAg@MIL-101 for One-Pot Cascade Reactions: Combination of Host–Guest Cooperation and Bimetallic Synergy in Catalysis. *ACS Catal.* **2015**, *5*, 2062–2069.
- (176) Chen, L.-N.; Li, H.-Q.; Yan, M.-W.; Yuan, C.-F.; Zhan, W.-W.; Jiang, Y.-Q.; Xie, Z.-X.; Kuang, Q.; Zheng, L.-S. Ternary Alloys Encapsulated within Different MOFs via a Self-Sacrificing Template Process: A Potential Platform for the Investigation of Size-Selective Catalytic Performances. *Small* **2017**, *13*, 1700683.
- (177) Guo, Z.; Xiao, C.; Maligal-Ganesh, R. V.; Zhou, L.; Goh, T. W.; Li, X.; Tesfagaber, D.; Thiel, A.; Huang, W. Pt Nanoclusters Confined within Metal–Organic Framework Cavities for Chemoselective Cinnamaldehyde Hydrogenation. *ACS Catal.* **2014**, *4*, 1340–1348.
- (178) Ahn, S.; Thornburg, N. E.; Li, Z.; Wang, T. C.; Gallington, L. C.; Chapman, K. W.; Notestein, J. M.; Hupp, J. T.; Farha, O. K. Stable Metal-Organic Framework-Supported Niobium Catalysts. *Inorg. Chem.* **2016**, *55*, 11954–11961.
- (179) Redfern, L. R.; Li, Z.; Zhang, X.; Farha, O. K. Highly Selective Acetylene Semihydrogenation Catalyzed by Cu Nanoparticles Supported in a Metal-Organic Framework. *Acsl Appl. Nano Mater.* **2018**, *1*, 4413–4417.
- (180) Peng, Y.; Geng, Z.; Zhao, S.; Wang, L.; Li, H.; Wang, X.; Zheng, X.; Zhu, J.; Li, Z.; Si, R.; et al. Pt Single Atoms Embedded in the Surface of Ni Nanocrystals as Highly Active Catalysts for Selective Hydrogenation of Nitro Compounds. *Nano Lett.* **2018**, *18*, 3785–3791.
- (181) Zhang, H.; Watanabe, T.; Okumura, M.; Haruta, M.; Toshima, N. Catalytically Highly Active Top Gold Atom on Palladium Nanocluster. *Nat. Mater.* **2012**, *11*, 49–52.
- (182) Wang, L.; Zhang, W.; Wang, S.; Gao, Z.; Luo, Z.; Wang, X.; Zeng, R.; Li, A.; Li, H.; Wang, M.; et al. Atomic-Level Insights in Optimizing Reaction Paths for Hydroformylation Reaction over Rh/CoO Single-Atom Catalyst. *Nat. Commun.* **2016**, *7*, 14036.
- (183) Duchesne, P. N.; Li, Z. Y.; Deming, C. P.; Fung, V.; Zhao, X.; Yuan, J.; Regier, T.; Aldalbahi, A.; Almarhoon, Z.; Chen, S.; Jiang, D. e.; Zheng, N.; Zhang, P. Golden Single-Atomic-Site Platinum Electrocatalysts. *Nat. Mater.* **2018**, *17*, 1033–1039.
- (184) Gao, C.; Chen, S.; Wang, Y.; Wang, J.; Zheng, X.; Zhu, J.; Song, L.; Zhang, W.; Xiong, Y. Heterogeneous Single-Atom Catalyst for Visible-Light-Driven High-Turnover CO<sub>2</sub> Reduction: The Role of Electron Transfer. *Adv. Mater.* **2018**, *30*, 1704624.
- (185) Nie, L.; Mei, D.; Xiong, H.; Peng, B.; Ren, Z.; Hernandez, X. I. P.; DeLariva, A.; Wang, M.; Engelhard, M. H.; Kovarik, L.; et al. Activation of Surface Lattice Oxygen in Single-Atom Pt/CeO<sub>2</sub> for Low-Temperature CO Oxidation. *Science* **2017**, *358*, 1419–1423.
- (186) Graciani, J.; Mudiyanselage, K.; Xu, F.; Baber, A. E.; Evans, J.; Senanayake, S. D.; Stacchiola, D. J.; Liu, P.; Hrbek, J.; Fernandez Sanz, J.; et al. Highly Active Copper-Ceria and Copper-Ceria-Titania Catalysts for Methanol Synthesis from CO<sub>2</sub>. *Science* **2014**, *345*, 546–550.
- (187) Chen, G.; Xu, C.; Huang, X.; Ye, J.; Gu, L.; Li, G.; Tang, Z.; Wu, B.; Yang, H.; Zhao, Z.; et al. Interfacial Electronic Effects Control the Reaction Selectivity of Platinum Catalysts. *Nat. Mater.* **2016**, *15*, 564–569.
- (188) Bruix, A.; Rodriguez, J. A.; Ramirez, P. J.; Senanayake, S. D.; Evans, J.; Park, J. B.; Stacchiola, D.; Liu, P.; Hrbek, J.; Illas, F. A New Type of Strong Metal-Support Interaction and the Production of H<sub>2</sub> through the Transformation of Water on Pt/CeO<sub>2</sub>(111) and Pt/CeO<sub>x</sub>/TiO<sub>2</sub>(110) Catalysts. *J. Am. Chem. Soc.* **2012**, *134*, 8968–74.
- (189) Chen, W.; Ma, Y.; Li, F.; Pan, L.; Gao, W.; Xiang, Q.; Shang, W.; Song, C.; Tao, P.; Zhu, H.; et al. Strong Electronic Interaction of Amorphous Fe<sub>2</sub>O<sub>3</sub> Nanosheets with Single-Atom Pt toward Enhanced Carbon Monoxide Oxidation. *Adv. Funct. Mater.* **2019**, *29*, 1904278.
- (190) Liu, K.; Zhao, X.; Ren, G.; Yang, T.; Ren, Y.; Lee, A. F.; Su, Y.; Pan, X.; Zhang, J.; Chen, Z.; et al. Strong Metal-Support Interaction Promoted Scalable Production of Thermally Stable Single-Atom Catalysts. *Nat. Commun.* **2020**, *11*, 1263.
- (191) Chen, S.; Li, M.; Gao, M.; Jin, J.; van Spronsen, M. A.; Salmeron, M. B.; Yang, P. High-Performance Pt-Co Nanoframes for Fuel-Cell Electrocatalysis. *Nano Lett.* **2020**, *20*, 1974–1979.
- (192) Luo, M.; Zhao, Z.; Zhang, Y.; Sun, Y.; Xing, Y.; Lv, F.; Yang, Y.; Zhang, X.; Hwang, S.; Qin, Y.; et al. PdMo Bimettallene for Oxygen Reduction Catalysis. *Nature* **2019**, *574*, 81–85.
- (193) Tian, X.; Zhao, X.; Su, Y. Q.; Wang, L.; Wang, H.; Dang, D.; Chi, B.; Liu, H.; Hensen, E. J. M.; Lou, X. W.; et al. Engineering Bunched Pt-Ni Alloy Nanocages for Efficient Oxygen Reduction in Practical Fuel Cells. *Science* **2019**, *366*, 850–856.
- (194) Abild-Pedersen, F.; Greeley, J.; Norskov, J. K. Understanding the Effect of Steps, Strain, Poisons, and Alloying: Methane Activation on Ni Surfaces. *Catal. Lett.* **2005**, *105*, 9–13.
- (195) Jaramillo, T. F.; Jorgensen, K. P.; Bonde, J.; Nielsen, J. H.; Horch, S.; Chorkendorff, I. Identification of Active Edge Sites for Electrochemical H<sub>2</sub> Evolution from MoS<sub>2</sub> Nanocatalysts. *Science* **2007**, *317*, 100–102.
- (196) Khan, M. U.; Wang, L.; Liu, Z.; Gao, Z.; Wang, S.; Li, H.; Zhang, W.; Wang, M.; Wang, Z.; Ma, C.; et al. Pt<sub>3</sub>Co Octapods as Superior Catalysts of CO<sub>2</sub> Hydrogenation. *Angew. Chem., Int. Ed.* **2016**, *55*, 9548–9552.
- (197) Du, X.; Huang, J.; Zhang, J.; Yan, Y.; Wu, C.; Hu, Y.; Yan, C.; Lei, T.; Chen, W.; Fan, C.; Xiong, J. Modulating Electronic Structures of Inorganic Nanomaterials for Efficient Electrocatalytic Water Splitting. *Angew. Chem., Int. Ed.* **2019**, *58*, 4484–4502.
- (198) Ding, J.; Asta, M.; Ritchie, R. O. Melts of CrCoNi-based High-Entropy Alloys: Atomic Diffusion and Electronic/Atomic Structure from *ab initio* Simulation. *Appl. Phys. Lett.* **2018**, *113*, 111902.
- (199) Odbadrakh, K.; Enkhtor, L.; Amartaivan, T.; Nicholson, D. M.; Stocks, G. M.; Egami, T. Electronic Structure and Atomic Level Complexity in Al<sub>0.5</sub>TiZrPdCuNi High-Entropy Alloy in Glass Phase. *J. Appl. Phys.* **2019**, *126*, 095104.
- (200) Bu, L.; Zhang, N.; Guo, S.; Zhang, X.; Li, J.; Yao, J.; Wu, T.; Lu, G.; Ma, J. Y.; Su, D.; et al. Biaxially Strained PtPb/Pt Core/Shell Nanoplate Boosts Oxygen Reduction Catalysis. *Science* **2016**, *354*, 1410–1414.
- (201) Zhu, H.; Gao, G.; Du, M.; Zhou, J.; Wang, K.; Wu, W.; Chen, X.; Li, Y.; Ma, P.; Dong, W.; et al. Atomic-Scale Core/Shell Structure Engineering Induces Precise Tensile Strain to Boost Hydrogen Evolution Catalysis. *Adv. Mater.* **2018**, *30*, 1707301.
- (202) Ling, T.; Yan, D. Y.; Wang, H.; Jiao, Y.; Hu, Z.; Zheng, Y.; Zheng, L.; Mao, J.; Liu, H.; Du, X. W.; Jaroniec, M.; Qiao, S. Z. Activating Cobalt(II) Oxide Nanorods for Efficient Electrocatalysis by Strain Engineering. *Nat. Commun.* **2017**, *8*, 1509.
- (203) Liu, X.; Zhang, L.; Zheng, Y.; Guo, Z.; Zhu, Y.; Chen, H.; Li, F.; Liu, P.; Yu, B.; Wang, X.; Liu, J.; Chen, Y.; Liu, M. Uncovering the Effect of Lattice Strain and Oxygen Deficiency on Electrocatalytic Activity of Perovskite Cobaltite Thin Films. *Adv. Sci.* **2019**, *6*, 1801898.
- (204) Huang, H.; Jia, H.; Liu, Z.; Gao, P.; Zhao, J.; Luo, Z.; Yang, J.; Zeng, J. Understanding of Strain Effects in the Electrochemical Reduction of CO<sub>2</sub>: Using Pd Nanostructures as an Ideal Platform. *Angew. Chem., Int. Ed.* **2017**, *56*, 3594–3598.
- (205) Liu, J. X.; Su, H. Y.; Sun, D. P.; Zhang, B. Y.; Li, W. X. Crystallographic Dependence of CO Activation on Cobalt Catalysts: HCP versus FCC. *J. Am. Chem. Soc.* **2013**, *135*, 16284–16287.
- (206) Li, W. Z.; Liu, J. X.; Gu, J.; Zhou, W.; Yao, S. Y.; Si, R.; Guo, Y.; Su, H. Y.; Yan, C. H.; Li, W. X.; et al. Chemical Insights into the Design and Development of Face-Centered Cubic Ruthenium Catalysts for Fischer–Tropsch Synthesis. *J. Am. Chem. Soc.* **2017**, *139*, 2267–2276.

- (207) Hou, T.; Guo, R.; Chen, L.; Xie, Y.; Guo, J.; Zhang, W.; Zheng, X.; Zhu, W.; Tan, X.; Wang, L. Atomic-Level Insights in Tuning Defective Structures for Nitrogen Photofixation over Amorphous SmOCl Nanosheets. *Nano Energy* **2019**, *65*, 104003.
- (208) Hou, T.; Xiao, Y.; Cui, P.; Huang, Y.; Tan, X.; Zheng, X.; Zou, Y.; Liu, C.; Zhu, W.; Liang, S.; et al. Operando Oxygen Vacancies for Enhanced Activity and Stability toward Nitrogen Photofixation. *Adv. Energy Mater.* **2019**, *9*, 1902319.
- (209) Yang, J.; Guo, Y.; Lu, W.; Jiang, R.; Wang, J. Emerging Applications of Plasmons in Driving CO<sub>2</sub> Reduction and N<sub>2</sub> Fixation. *Adv. Mater.* **2018**, *30*, 1802227.
- (210) Christopher, P.; Xin, H.; Linic, S. Visible-Light-Enhanced Catalytic Oxidation Reactions on Plasmonic Silver Nanostructures. *Nat. Chem.* **2011**, *3*, 467–472.
- (211) Zhang, N.; Jalil, A.; Wu, D.; Chen, S.; Liu, Y.; Gao, C.; Ye, W.; Qi, Z.; Ju, H.; Wang, C.; et al. Refining Defect States in W<sub>18</sub>O<sub>49</sub> by Mo Doping: A Strategy for Tuning N<sub>2</sub> Activation towards Solar-Driven Nitrogen Fixation. *J. Am. Chem. Soc.* **2018**, *140*, 9434–9443.
- (212) Rudi, S.; Teschner, D.; Beermann, V.; Hetaba, W.; Gan, L.; Cui, C.; Giech, M.; Schloegl, R.; Strasser, P. pH-Induced versus Oxygen-Induced Surface Enrichment and Segregation Effects in Pt-Ni Alloy Nanoparticle Fuel Cell Catalysts. *ACS Catal.* **2017**, *7*, 6376–6384.
- (213) Ma, Y.; Miao, L.; Guo, W.; Yao, X.; Qin, F.; Wang, Z.; Du, H.; Li, J.; Kang, F.; Gan, L. Modulating Surface Composition and Oxygen Reduction Reaction Activities of Pt-Ni Octahedral NPs by Microwave-Enhanced Surface Diffusion during Solvothermal Synthesis. *Chem. Mater.* **2018**, *30*, 4355–4360.
- (214) Peng, H.; Xie, Y.; Xie, Z.; Wu, Y.; Zhu, W.; Liang, S.; Wang, L. Large-scale and Facile Synthesis of Porous High-entropy Alloy CrMnFeCoNi as an Efficient Catalyst. *J. Mater. Chem. A* **2020**, DOI: 10.1039/D0TA04940A.
- (215) Marimuthu, A.; Zhang, J.; Linic, S. Tuning Selectivity in Propylene Epoxidation by Plasmon Mediated Photo-Switching of Cu Oxidation State. *Science* **2013**, *339*, 1590–1593.
- (216) Zhou, L.; Martinez, J. M. P.; Finzel, J.; Zhang, C.; Swearer, D. F.; Tian, S.; Robatjazi, H.; Lou, M.; Dong, L.; Henderson, L.; Christopher, P.; et al. Light-driven Methane Dry Reforming with Single Atomic Site Antenna-Reactor Plasmonic Photocatalysts. *Nat. Energy* **2020**, *5*, 61–70.
- (217) Hu, C.; Chen, X.; Jin, J.; Han, Y.; Chen, S.; Ju, H.; Cai, J.; Qiu, Y.; Gao, C.; Wang, C.; et al. Surface Plasmon Enabling Nitrogen Fixation in Pure Water through a Dissociative Mechanism under Mild Conditions. *J. Am. Chem. Soc.* **2019**, *141*, 7807–7814.
- (218) Marschall, R. Semiconductor Composites: Strategies for Enhancing Charge Carrier Separation to Improve Photocatalytic Activity. *Adv. Funct. Mater.* **2014**, *24*, 2421–2440.
- (219) Li, M.; Zhang, N.; Long, R.; Ye, W.; Wang, C.; Xiong, Y. PdPt Alloy Nanocatalysts Supported on TiO<sub>2</sub>: Maneuvering Metal-Hydrogen Interactions for Light-Driven and Water-Donating Selective Alkyne Semihydrogenation. *Small* **2017**, *13*, 1604173.
- (220) Ran, J.; Jaroniec, M.; Qiao, S. Z. Cocatalysts in Semiconductor-based Photocatalytic CO<sub>2</sub> Reduction: Achievements, Challenges, and Opportunities. *Adv. Mater.* **2018**, *30*, 1704649.
- (221) Hou, T.; Peng, H.; Xin, Y.; Wang, S.; Zhu, W.; Chen, L.; Yao, Y.; Zhang, W.; Liang, S.; Wang, L. Fe Single-Atom Catalyst for Visible-Light-Driven Photofixation of Nitrogen Sensitized by Triphenylphosphine and Sodium Iodide. *ACS Catal.* **2020**, *10*, 5502–5510.